NORTHWESTERN UNIVERSITY

Realization of Radio-Krypton Dating With an Atom Trap

A DISSERTATION

SUBMITTED TO THE GRADUATE SCHOOL
IN PARTIAL FULFILLMENT OF THE REQUIREMENTS

for the degree

DOCTOR OF PHILOSOPHY

Field of Physics and Astronomy

By

Xu Du

EVANSTON, ILLINOIS

June 2003

ABSTRACT

Realization of Radio-Krypton Dating With an Atom Trap

Xu Du

An atom trap system for practical ^{81}Kr-dating has been developed. Calibration of the system has been accomplished. With this system, ^{81}Kr-dating of ancient groundwater has been realized.

^{81}Kr ($t_{1/2} = 230$ kyr, isotopic abundance $\sim 5\times10^{-13}$) is a long-lived cosmogenic isotope, ideal for dating old groundwater and ice in the range of 50,000 years to a million years. Due to the extremely low isotopic abundance of ^{81}Kr (~ 1000 ^{81}Kr atoms are contained in 1 liter of modern ice or groundwater), analysis of ^{81}Kr at or below the atmospheric isotopic abundance has been an experimental challenge.

This work presents the development of the Atom Trap Trace Analysis method for practical ^{81}Kr-dating. This method is based on laser manipulation of neutral atoms. The atom trap system is capable of detecting individual ^{81}Kr and ^{85}Kr atoms with an isotopic abundance as low as 0.1 parts per trillion. With the counting efficiency of 2×10^{-4} and the required sample size of below 100 μl STP of krypton gas, the system has met the requirement of implementing ^{81}Kr-dating of ancient groundwater. A demonstration of the system capability on quantitative measurements has been performed by analyzing the ratios of ^{85}Kr/^{81}Kr in a group of Kr samples prepared by an Environmental Science group

at the University of Bern. Among these samples derived from young (age less than 70 years) air samples, the ^{81}Kr/Kr ratios are expected to be identical while the ^{85}Kr/Kr ratios (measured with Low Level Counting at Bern group) are expected to vary. A good agreement between our results and LLC results has demonstrated the validity of our method.

The system has been used to date the ancient groundwater of the Nubian Aquifer in Egypt. Two groundwater samples have been analyzed and their residence times are 596±195 kyr and 474±89 kyr, respectively.

ACKNOWLEDGMENTS

This thesis project was performed in Dr. Zheng-Tian Lu's Atom Trap group at Physics Division, Argonne National Laboratory. In presenting this thesis, I wish to express my sincere thanks to those who have given me support and encouragement during 4 years of study and work at Argonne.

First of all, I would like to thank my thesis advisor, Dr. Zheng-Tian Lu, for his guidance and support throughout my thesis project. His expertise in the field of atomic physics improved my research skills and strengthened my ability to solve problems. Meanwhile, his insight, persistence and love of science show me how to become a successful young scientist.

I thank Professor Hui Cao for being my dissertation committee chair. I thank other committee members, Professors Ralph Segel and Ron Taam, for their helpful suggestions on my dissertation.

Special thanks go to Dr. Linda Young at Chemistry Division, Argonne National Laboratory. Her suggestions and help are invaluable to this project and myself.

I am grateful to Kevin Bailey and Tom O'Connor for their strong technical support.

I enjoy working with Dr. Peter Mueller, Dr. Iain Moore, Dr. Elaine Schulte, and Li-Bang Wang in Atom Trap group. Discussions among us are always fruitful.

I thank former group members Dr. Yi-Min Li and Dr. Chun-Yen Chen for their personal and academic help in my first year at Argonne.

I thank Dr. Philippe Collon at Columbia University for providing beautiful diagrams of AMS. I thank Dr. Brian DeMarco at NIST for useful suggestions on tapered amplifiers.

Finally, I thank Medium Energy Physics (MEP) group chief Dr. Roy Holt for his encouragement and other MEP group members for teaching me nuclear physics.

To

my parents

and

Lin Lu

Table of Contents

List of Figures

List of Tables

1 Radiocarbon Dating and Beyond

Much can be learned from the analysis of the ubiquitous long-lived radioactive isotopes. In the late 1940's, W. Libby and coworkers first detected the cosmogenic isotope ^{14}C ($t_{1/2} = 5.7\times10^{3}$ yr, isotopic abundance $\approx 1\times10^{-12}$) in nature and demonstrated that such analysis could be used for archaeological dating [1, 2]. Since then, two well-developed methods, Low-Level Counting (LLC) and Accelerator Mass Spectrometry (AMS), have been used to analyze ^{14}C and many other radioisotopes and to extract valuable information encoded in the production, transport, and decay processes of these isotopes.

By far ^{14}C is one of the most widely used trace isotopes. In section 1.1, taking ^{14}C as an example of radioisotopes, we introduce the principles of trace analysis and describe the applications of trace analysis in archeology and environmental research. Though ^{14}C-dating is very successful, its half-life dictates that the method can only be used in the time range from a thousand years up to 50,000 years. In section 1.2, we discuss three noble gas radioisotopes (^{81}Kr, ^{85}Kr and ^{39}Ar), which can be used in many areas beyond the reach of ^{14}C-dating, and significantly expand the applications of trace analysis in earth sciences.

1.1 ^{14}C-dating

^{14}C is formed in the upper atmosphere through the cosmic-ray neutron activation of ^{14}N,

$$^{14}N + n \rightarrow ^{14}C + p$$

It takes months for the produced ^{14}C to be oxidized to $^{14}CO_2$ and to enter the biosphere through the photosynthesis and food chain. Plants and animals that utilize carbon in the biological food chains take up ^{14}C during their lifetime and the

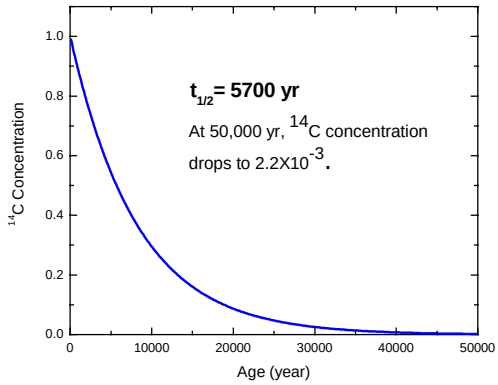

Figure 1.1 Decay curve of ^{14}C. At 50,000 year, ^{14}C concentration drops to 2.2×10^{-15}, and ^{14}C-dating ceases to be effective.

concentration of ^{14}C within them is identical to that in the atmosphere. As soon as a plant or animal dies, the process of carbon uptake stops and no more ^{14}C atoms can enter them (the inner rings of a tree stop taking ^{14}C before the tree dies). Therefore, concentration of ^{14}C starts decreasing due to ^{14}C radioactive decay ($^{14}C \rightarrow ^{14}N + e^- + \bar{\nu}_e$). By measuring the concentration of ^{14}C in a sample of a dead plant or animal and comparing it with that in the modern atmosphere, one can determine the sample age by

$$t = \frac{t_{1/2}}{\ln 2} \ln\left(\frac{A_0}{A(t)}\right) \qquad (1.1)$$

where t is the sample age; $t_{1/2}$ is the half-lifetime of ^{14}C (=5700 yr); A_0 is the isotopic abundance of ^{14}C in the atmosphere; $A(t)$ is the isotopic abundance of ^{14}C in the sample. Figure 1.1 shows the decay curve of ^{14}C.

Here one assumes that the atmospheric ^{14}C concentration in the past has been the same as the present. Unfortunately, this assumption is not true. By measuring the ^{14}C concentration of known-age tree rings, people found that the age directly derived from ^{14}C concentration measurement could vary from the real age of the tree rings up to a maximum of $\pm 10\%$. The results suggested that atmospheric concentration of ^{14}C was not constant during the past several thousand years and that age calibration is needed in order

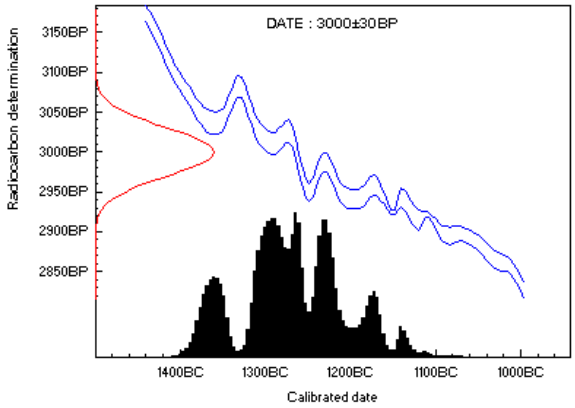

Figure 1.2 A radiocarbon calibration example. The vertical axis shows radiocarbon concentration expressed in years "before present" and the horizontal axis shows calendar years (derived from the tree ring data). The pair of blue curves shows the radiocarbon measurements on the tree rings (plus and minus one standard deviation) and the red curve on the left indicates the radiocarbon concentration in the sample. The black histogram shows possible ages for the sample (the higher the histogram the more likely the more likely that age is). The results of this calibration are often given as an age range. In this case, with 95% confidential, the sample originates between 1390 BC and 1130 BC. (Courtesy of http://www.c14dating.com/)

to acquire a reliable age information of the sample. Figure 1.2 shows a radiocarbon calibration example.

^{14}C can be used to date a sample in the range from a few hundred years to 50,000 years. This dating range is limited by the half-life of ^{14}C. At around 50,000 years, or 9 half-lives of ^{14}C, the isotopic abundance of ^{14}C in the sample drops to ~10^{-15}, or below 0.2% of that in modern atmosphere (shown in Figure 1.1). Two reasons make ^{14}C-dating at the level of 10^{-15} nearly impossible: one is that ^{14}C is difficult to detect at this extremely low abundance level; the other is that small contamination of ^{14}C from modern atmosphere can introduce a large systematic error in the age determination.

Since the half-life of ^{14}C is comparable to the history of human civilization, ^{14}C-dating has been a very successful age-determination method in archeology. With the technique of Accelerator Mass Spectrometry (AMS), ^{14}C-dating of milligram samples can reach a precision of 1%. One famous example is ^{14}C-dating of the Shroud of Turin [3, 4]. The Shroud was believed by many to be the burial cloth of Christ. Three AMS laboratories carried out independent ^{14}C-dating measurement on a small piece of linen from the Shroud, with a total weight of about 50 mg. Their results were in excellent agreement and showed that the age of the Shroud was medieval with an age of 1260-1390 AD (>95% confidence) rather than originating from the time of Christ.

^{14}C-dating, along with the trace analysis of many other radioisotopes, also has a wide range of applications in earth sciences [5, 6, 7, 8].

(1) Dating groundwater. Groundwater is an increasingly important water source in arid and semi-arid regions [6]. In the United States, groundwater is used for drinking by more

than 50% of the population, including almost everyone who lives in rural areas. Therefore it is important and necessary for people to quantitatively understand the subsurface water reservoirs, including their sizes and flow characteristics. This can be addressed by dating groundwaters. Age of groundwater is defined as the period since the

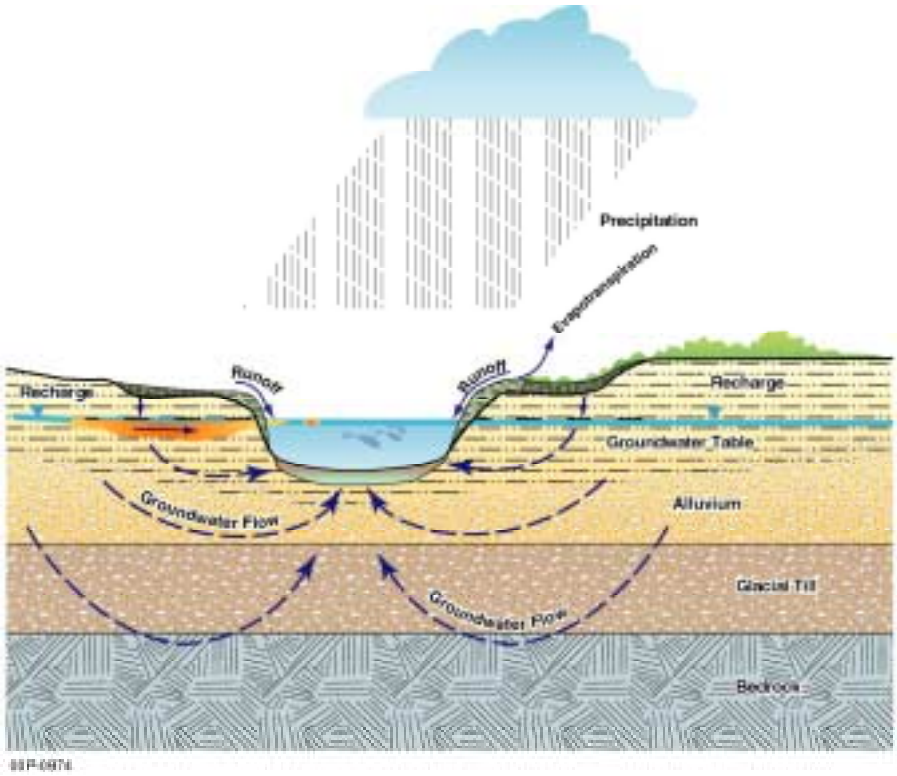

Figure 1.3 Schematic layout of a groundwater system. Groundwater is water that is stored underground in cracks and spaces in soil, sand and rocks. The area where groundwater is found is called the saturation zone. The top of this zone is called the water table. The layers of soil, sand and rocks, among which the groundwater is stored and moves, are called aquifers. Water in aquifers can come to the surface naturally through a spring or be extracted through a well. Groundwater is recharged by rain and melting snow.

water went subsurface and was isolated from the atmosphere. Figure 1.3 shows the schematic layout of a groundwater system.

The other application of dating old groundwater is to help characterize the sites of nuclear waste disposal [9]. The safety of the permanent radioactive waste burial sites has been attracting public interests and concerns. For example, during the past 50 years, the US has accumulated 5.5 million cubic meters of nuclear waste. All of the storage arrangements of those wastes are temporary (20 to 50 years). Although Congress has recently [10] approved that most nuclear wastes should be deposited in Yucca Mountain in Nevada, what may happen ten thousand–or even a million–years in the future is still a serious concern because the natural process will eventually redistribute the waste materials and possibly spread the nuclear contamination to the local neighborhood. Dating groundwater can help generate models of the groundwater flow system near the site, which are necessary to assess long-term environmental impact.

^{14}C-dating is by now the most widely used method [7, 8] to date the groundwater in the range from a few hundred years up to 50,000 years. CO_2 in the atmosphere can dissolve into the water in the form of HCO_3^- . Once the water goes underneath and is isolated from the atmosphere, ^{14}C concentration starts decreasing due to the ^{14}C decay, similar to the case of living plants or animals. Ideally, by measuring the concentration of ^{14}C in the water and using equation (1.1), one can determine the age of the groundwater. However, due to the complex geochemistry processes of carbon in the groundwater system, there may be many other sinks and sources of carbon, which could have ^{14}C contribution to the groundwater at the various concentration levels. For instance, Carbonate minerals with a much lower ^{14}C concentration level can dissolve into the

groundwater and as a consequence will give an older age of the groundwater. Therefore, geochemical models are necessary to interpret ^{14}C-dating results. But even with modelling, the complicated and difficult analysis of the data of ^{14}C-dating could lead to errors in the age determination of the groundwater.

(2) Dating ancient ice. Ancient-ice cores have provided unique information about the history of the earth's climate [11] and have helped to develop climate models to predict the future weather. One such example is the Antarctica ice core. In 1998, the Russian-French-American ice-coring team at the Vostok station in eastern Antarctica reached a depth of 3623 m in the ice. The achievement provides a continuous ice core record spanning an estimated 420,000 years [12, 13]. Figure 1.4 shows the pictures of drilling ice cores on site. Figure 1.5 shows the pictures of ice core storage at National Ice Core Laboratory at Boulder, Colorado. A typical ice core is approximately 12 cm in diameter and weighs a few kilograms. The trapped air bubbles and dusts supply the important clues to the ancient climate. Scientists determined the composition (such as greenhouse gases CO_2, CH_4) of the ancient atmospheres through direct analysis of trapped air bubbles in ice. They analyzed the isotopic composition ($^{18}O/^{16}O$ ratio and ratio of deuterium to hydrogen) of the ice to study the temperature changes in the past.

The pattern of climate change recorded in the ice core supports the orbital theory of ice ages [14], in which the timing of glaciation cycles (~20,000 years in a cycle) is attributed to the periodicity of changes in the shape of the Earth's orbit (eccentricity), the tilt of the Earth's axis (obliquity) and the timing of its closest approach to the Sun (precession). The ice core data on greenhouse gases led scientists to conclude that these gases play a

(a)

(b)

(c)

Figure 1.4 Drilling the ice core. (a) Drill dome at the GISP2 (Greenland Ice Sheet project Two) site in central Greenland; (b) setting up the drill; (c) Laying out core containers for packing (Courtesy of http://nicl.usgs.gov)

significant role in the glacial-interglacial climate changes. At the last glacial maximum (21,000 years before present), CO_2 is estimated to be 190-200 ppm, compared with the 270-280 ppm preindustrial average for the Holocene period (last 10,000 years). The warming that occurred between the glaciation and the Holocene period was approximately 10 degrees over Antarctica or 4-5 degrees averaged globally. CO_2 in the modern atmosphere is about 360 ppm, most of the increase happened in the past 50 years. Some scientists believe that the increase in greenhouse gases is the cause of globe warming. More data on the ice core will help generate more realistic models of the climate.

(a)

(b)

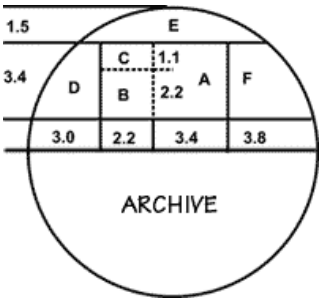

(c)

Figure 1.5 Ice core storage. **(a)** U.S. National Ice Core Laboratory currently houses over 14,000 meters of ice cores from 34 drill sites in Greenland, Antarctica, and high mountain glaciers in the Western United States; **(b)** Spot checking the condition of a newly-arrived core; **(c)** A typical ice core is about 12 cm in diameter. (Courtesy of http://nicl.usgs.gov)

The crucial prerequisite in the study of ice cores is the accurate age determination of the samples [14]. Without these data, scientists could not build an overall chronology in which to place their measurements. Ice layers can be analyzed in much the same way that yearly growth rings can be used to determine the age of a tree. For the ice core of younger than 11,500 years, layer counting is correct to within 1%. The ice layers up to

50,000 years still appear to be good enough to count, although the accuracy is poorer in the ice from colder times. It is becoming difficult to tell the layers of the deep ice cores with over 100,000 years because the ice layers start to spread and become thin due to compression. Consequently, thinning and diffusion make it impossible to count the layers beyond 100,000 years. Currently, the age of older-ice cores is estimated based on ice flow modeling using electrical conductivity measurements, ice accumulation changes, and correlation with other paleoclimatic records.

^{14}C-dating can be used to determine the age of the ice in the range of a few hundred years to 50,000 years [15]. The principle is to measure the concentration of ^{14}C in the trapped CO_2 in the ice core. Note that the dating range of ^{14}C-dating is comparable to that of layer counting. It is more desirable to find a new method which can date the ice beyond 100,000 years.

(3) Dating of "Great Conveyor Belt". "Great Conveyor Belt" [16] illustrates the global ocean circulation as shown in Figure 1.6. The conveyor belt is a giant loop that spans most of the world's oceans - cold water moves from north to south along the Atlantic sea floor, while warm water travels the opposite way near the surface. A complete cycle takes about 1,000 years as determined by ^{14}C-dating. The water in the conveyor belt carries a great amount of heat, making it crucial to the global climate system. Melting ice after the most recent Ice Age is thought to have halted the conveyor, causing sudden and massive shifts in climate. Some scientists worry that melting of icebergs as a result of global warming could lead to the same effect.

The oceans store much more CO_2 than the atmosphere. Approximately 93% of ^{14}C on Earth is stored in the oceans [17]. The ocean surface water has the same ratio of ^{14}C to

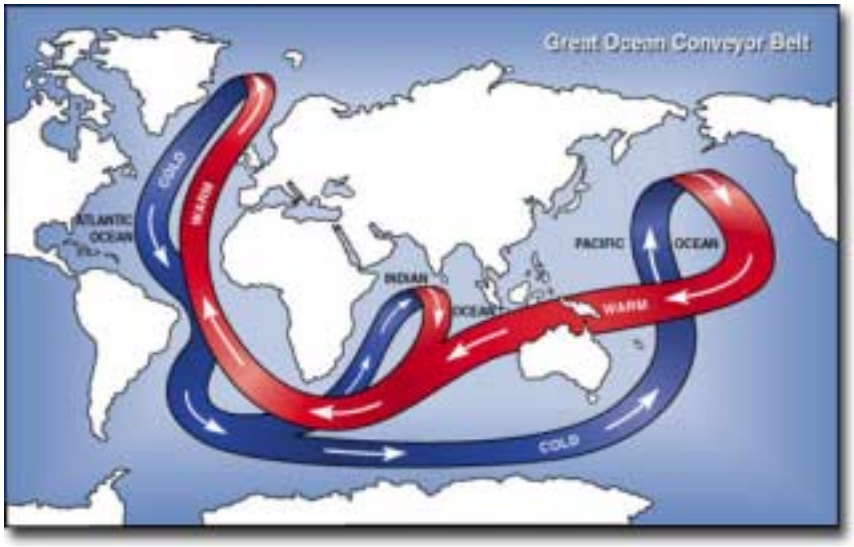

Figure 1.6 Conceptual illustration of the ocean conveyor belt circulation illustrates the 1,000-year long cycle. Warm, shallow water is chilled in the far North Atlantic, grows saltier and sinks. The cold, salty current flows south near the bottom, creating a northward surface layer flow of the warm, less salty water. (Courtesy of http://www.anl.gov/OPA/whatsnew/oceancurrents.htm)

carbon as in the atmosphere, while the deeper water has a reduced ratio due to the ^{14}C decay. By measuring the ratio of ^{14}C to carbon, one can determine the age of the ocean water, i.e. how long the water has been isolated from the atmosphere. A detailed study of age differences between surface and deep water around the world helps understand the pattern of the global circulation.

1.2 Noble Gas Radioisotopes

Since noble gases are chemically inert, dating of their radioisotopes is immune to the chemical interactions which can alter the isotopic abundance in the transport processes [18]. Therefore noble gas radioisotope tracers have advantages over the reactive element tracers (such as ^{14}C) that, the interpretation of their abundance data is much simpler and consequently would lead to more accurate age information of the sample.

The time range of ^{14}C-dating is from a few hundred years to 50,000 years. In order to cover the dating range from the present to a few million years, more radioisotope tracers are needed. There are three long-lived noble gas radioisotopes which are believed to be the ideal tracers to fill the gaps; ^{85}Kr ($t_{1/2} = 10.76$ yr) is used as tracer in the time range

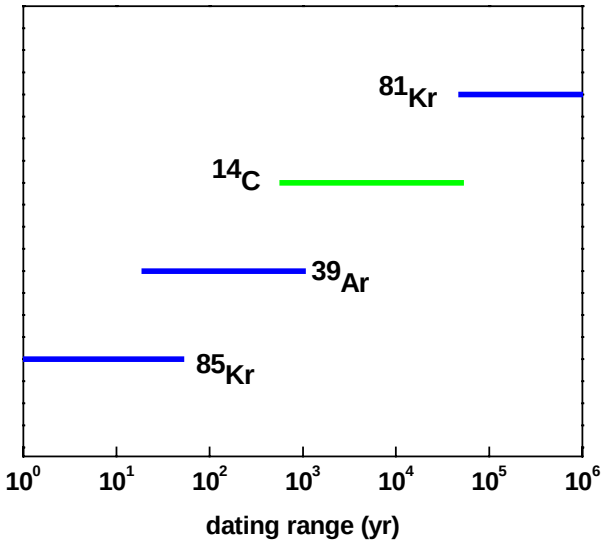

Figure 1.7 Dating time range of ^{14}C and three long-lived noble-gas radioisotopes (^{81}Kr, ^{85}Kr, ^{39}Ar).

from the present to 50 years, ^{39}Ar ($t_{1/2} = 268$ yr) is used between 40 years to 1,000 years,

^{81}Kr ($t_{1/2} = 230$ kyr) can be used in the range from 50,000 years to a million years. A dating time range diagram for ^{14}C and the three long-lived radioisotopes are shown in Figure 1.7.

1.2.1 ^{81}Kr

^{81}Kr ($t_{1/2} = 2.3\times10^{5}$ yr, isotopic abundance = 6×10^{-13}) is mainly produced in the upper atmosphere by cosmic-ray induced spallation and neutron activation of stable krypton isotopes [18]. As a noble gas, ^{81}Kr is well mixed in the atmosphere and forms a homogeneous atmospheric isotopic abundance. In addition, due to the long half-life, short-term fluctuations in cosmic-ray flux and the production of ^{81}Kr, are smoothed out over time. Human activities in nuclear fission have a negligible effect on the abundance of ^{81}Kr, largely because the stable ^{81}Br shields ^{81}Kr from β-decay feeding through more neutron-rich mass-81 fission products. These unique characteristics, along with the chemical inertness of krypton, make ^{81}Kr an ideal tracer to be used in the range of 50,000 years to a million years [6, 8].

For the time scale of 10^4 - 10^6 years, so far geologists have usually used the other radioisotope ^{36}Cl ($t_{1/2} = 3.01\times10^{5}$ yr, isotopic abundance = 7×10^{-13}), but the complex subsurface ^{36}Cl production makes the data analysis very difficult and inaccurate. Unlike ^{36}Cl, the anthropogenic and subsurface production of ^{81}Kr is negligible compared with the atmospheric concentration of ^{81}Kr which is expected to be constant.

^{81}Kr can be used to date ancient ice [11]. As we discussed above, beyond the range of 50,000 years, layer counting is not possible and ice flow modeling has been applied to estimate the age of the ice core. But for most cases, many input parameters of the model, such as electrical conductivity measurements and ice accumulation changes, are not well known. As a consequence, the estimated ages are controversial. ^{81}Kr-dating promises to offer a new reliable tool to determine the age of the old-ice core. Currently, the oldest-ice core extracted from Antarctica is estimated to be roughly 420,000 years old, which is within ^{81}Kr-dating range.

1.2.2 ^{85}Kr

^{85}Kr ($t_{1/2} = 10.76$ yr, isotopic abundance = 2×10^{-11}) is a product of nuclear fission processes [18, 19]. ^{235}U (or ^{239}Pu) nucleus splits into less massive nuclei (including ^{85}Kr) and a few neutrons. The production probability of ^{85}Kr per fission is about 0.3%. Sources of ^{85}Kr include nuclear-bomb testing, nuclear reactors, and the release of ^{85}Kr during the reprocessing of fuel rods from nuclear reactors. Since 1950's, ^{85}Kr abundance has steadily increased by six orders of amplitude. The radioactivity of ^{85}Kr in air over the Northern Hemisphere in 1990 was approximately 50 dpm/cc (decays per minute per cubic centimeter krypton) at STP (Standard Temperature and Pressure).

^{85}Kr can be used to date young groundwater [8]. Similar to ^{81}Kr, ^{85}Kr is not subject to the chemical interactions that can change its concentration in the subsurface water. Moreover, people have kept a thorough record of ^{85}Kr concentration in the atmosphere since 1950's. Therefore, ^{85}Kr holds a considerable promise as a tracer for dating the

young groundwater (less than 50 years). ^{85}Kr can also be used to indicate the mixing of old groundwater and young groundwater. Since the concentration of ^{85}Kr in the groundwater before 1950's is six orders of magnitude lower than that of the modern groundwater, any measurable concentration of ^{85}Kr in the old groundwater will show the contamination of the groundwater sample from the modern atmosphere, or the diffusion of the young groundwater into the old groundwater.

The other interest of ^{85}Kr is to be used as a tracer to monitor the nuclear-fuel reprocessing activities, which separate ^{239}Pu from spent nuclear fuel [19]. Since nuclear-fuel reprocessing contributes most of the ^{85}Kr in the atmosphere, the atmospheric concentration of ^{85}Kr can be a reliable indicator of global plutonium stockpiles, and therefore monitoring ^{85}Kr can help verify compliance to the nuclear Non-Proliferation Treaty. In addition, ^{85}Kr can serve as a leak sensor to check the seals of nuclear fuel cells and nuclear waste containers since it, as a noble gas, can diffuse through tiny cracks in the walls.

1.2.3 ^{39}Ar

^{39}Ar ($t_{1/2} = 268$ yr, isotopic abundance = 8×10^{-16}) is produced in the upper atmosphere by comic-ray induced neutron activation of ^{40}Ar [18]. Similar to ^{81}Kr, the major reservoir for ^{39}Ar is the atmosphere and the contributions from human activities with nuclear fission is negligible. The most interest in ^{39}Ar is to use it as a sensitive tracer for studying ocean circulation and mixing because the 268-year half-life of ^{39}Ar fits well into the timescale of the global and regional ocean currents.

^{14}C-dating has been the main method used to trace the ocean currents [17]. But since the half-life of ^{14}C is much longer than the typical timescale of ocean current, the difference in the concentration of ^{14}C between modern ocean water and 100 year old is only about 2%, which limits the accuracy of age determination [20, 21]. While ^{39}Ar has an almost perfect half-life to match the time scale of the ocean currents, a large difference in concentration of ^{39}Ar between the ocean water of different ages makes the more accurate age-determination measurement feasible. Moreover, the chemical inertness simplifies the data analysis of ^{39}Ar [20].

2 Methods for Trace Analysis of Long-lived Noble Gas Radioisotopes

The applications discussed in Chapter 1 are both important and attractive, but the task of analyzing ^{81}Kr ($t_{1/2}$ = 230 kyr, $I.A. = 6\times10^{-13}$), ^{85}Kr ($t_{1/2}$ = 10.76 yr, $I.A. = 2\times10^{-11}$) or ^{39}Ar ($t_{1/2}$ = 268 yr, $I.A. = 8\times10^{-16}$) at or below the atmospheric level has been a challenge to experimental analysts [22]. For example, due to the extremely low isotopic abundance of ^{81}Kr, only roughly 1000 ^{81}Kr atoms are contained in one liter of modern water or ice, therefore a very high overall efficiency is needed to analyze ^{81}Kr at the ppt level (parts per trillion). In the following two sections, we will review the previously existing analytical methods.

2.1 Low Level Counting (LLC) [23]

Radioisotopes decay in various ways including α-decay, β-decay, or electron-capture ($^{81}Kr + e^- \rightarrow {}^{81}Br + \nu_e + \gamma$; $^{85}Kr \rightarrow {}^{85}Rb + e^- + \bar{\nu}_e$; $^{39}Ar \rightarrow {}^{39}K + e^- + \bar{\nu}_e$). A single decay event releases energy in the range of 10^4 - 10^7 eV, and can be readily detected with a scintillation counter or a proportional counter with high efficiency (>50%). The overall counting efficiency is usually determined by the fraction of the decayed atoms in the sample during the detection period t_D. The shorter the half-life $t_{1/2}$, the higher the counting efficiency η. In principle, the counting efficiency can approach unity if the counting period is several times longer than the half-life of the radioisotope. However, in

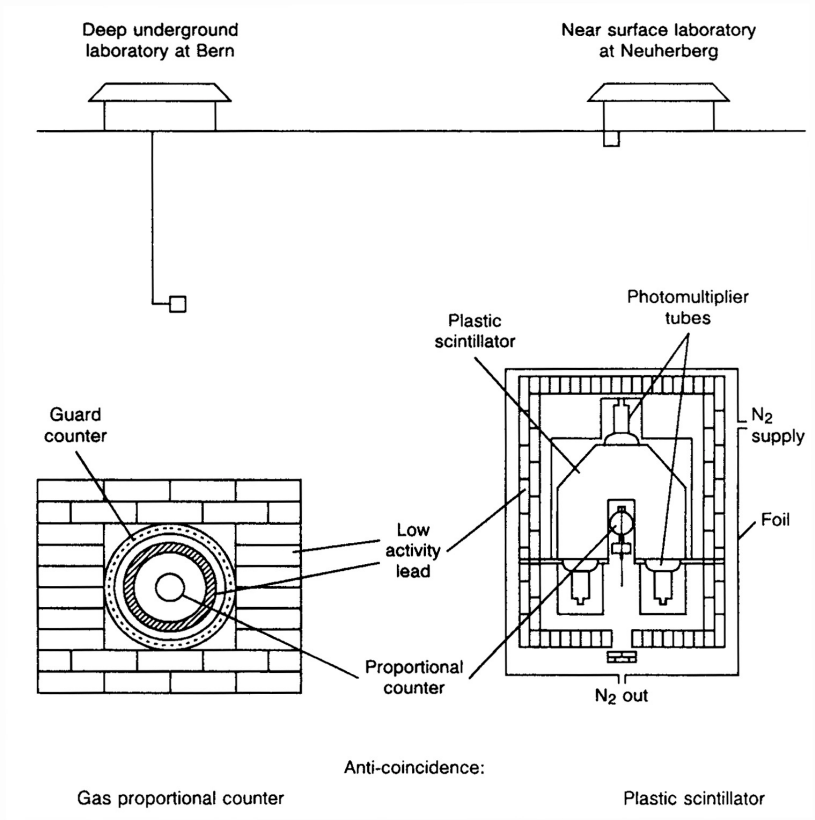

Figure 2.1 Low level counting. In the LLC technique, various efforts have been undertaken in order to reduce the radioactive background. (1) operating underground laboratory; (2) use of low-level radioactive construction material for detector and shield; (3) application of efficient anticoincidence detection system

reality this is impractical for counting the decay of long-lived isotopes. The counting efficiency can be calculated by $\eta \approx \ln 2 \frac{t_D}{t_{1/2}}$ when $t_D << t_{1/2}$. For example, in one week of counting, approximately 10^{-3} of ^{85}Kr, 10^{-7} of ^{81}Kr or 10^{-5} of ^{39}Ar in a sample decays.

LLC is often performed in a specially designed underground laboratory [24], as shown in Figure 2.1, in order to avoid the radioactive background due to cosmic-rays and the radioactivity present in the common construction materials. Environmental samples

usually contain other radioactive isotopes, whose concentrations can be reduced either by chemical purification, or in the case of short-lived impurities, by waiting.

Thus far, only LLC has been used to analyze ^{85}Kr in groundwater samples and ^{39}Ar in ocean and groundwater samples [23, 24]. For ^{85}Kr-dating, LLC requires 300 liters of water sample, which yields about 0.02 cm^3 STP of krypton and a counting rate of 1400 counts/day (with a detector counting efficiency of 70%). The standard counting time for ^{85}Kr-dating is about one week. For ^{39}Ar-dating, LLC measurement needs 2000 liters of water sample, which yields about 0.7 liter STP of argon and a counting rate of 70 counts/day (with a detector counting efficiency of 70%). The standard counting time for ^{39}Ar-dating is about 6 weeks. Currently LLC is the dominant method for trace analysis of ^{85}Kr and ^{39}Ar.

LLC was used to analyze ^{81}Kr for the first time [25] at the University of Bern, Switzerland. Two liters of pre-bomb krypton was used and more than 1,300 counts of ^{81}Kr were accumulated over 100 hours. But this is no longer possible due to the overwhelming background from decay of ^{85}Kr, which cannot be separated chemically from ^{81}Kr.

2.2 Accelerator Mass Spectrometry [26]

When analyzing long-lived isotopes, atom counting has a number of advantages over decay counting. The efficiency and speed of atom counting is not fundamentally limited

by the long lifetime of the isotope, nor is it affected by radioactive background in the environment or in the sample.

The widely used atom-counting method is mass spectrometry, which separates and detects individual ions of a chosen charge-to-mass ratio. This method is successful in routine trace analysis, but it is in general not suitable for analysis of radioactive isotopes whose isotopic abundances are less than 10^{-9}. This is primarily due to the contamination from the neighboring isotopes or isobars, which have close charge-to-mass ratio. For example, if $(^{14}C)^{+6}$ is used in mass spectrometry, there will be unavoidably much more abundant $(^{14}N)^{+6}$ in the beam to flood out the signal of $(^{14}C)^{+6}$.

It was realized in the late 1970's that the isobaric contamination problem can be solved in some cases by performing mass spectrometry with a high energy (~MeV) beam from an accelerator [27, 28], as shown in Figure 2.2. First, molecular isobars can be eliminated by passing the accelerated beam through a thin foil where the molecules disintegrate. Second, some atomic isobars can be eliminated by exploiting the stability property of the negative ions that are used in the first acceleration stage of a tandem accelerator. For example, $^{14}N^-$, the only abundant isobar of $^{14}C^-$, is not stable and, as a consequence, is not produced or accelerated. Third, with high-energy ions, more discriminatory ion detection techniques such as energy-loss measurement can be applied to help identify the ions of the certain isotopes and therefore further reduce the effect of isobaric contamination.

As a result of these advantages, AMS has replaced LLC as the standard method of ^{14}C-dating [29]. However, since krypton and argon atoms do not form negative ions, their

long-lived radioisotopes cannot be analyzed at the standard AMS facilities that employ tandem accelerators. Recent works [30, 31, 32] have shown that, by using an Electron Cyclotron Resonance (ECR) ion source to produce positive ions and by using a higher energy (~4 GeV) accelerator to separate isobars, these noble gas isotopes can be analyzed with AMS. The development of AMS analysis of ^{81}Kr culminated in the first demonstration of ^{81}Kr-dating of old groundwater. Using the MSU Superconducting Cyclotron, as shown in Figure 2.3, Collon *et al.* realized ^{81}Kr-dating and determined the ages of groundwater, in the range between 200 kyr and 400 kyr, at several sites in the

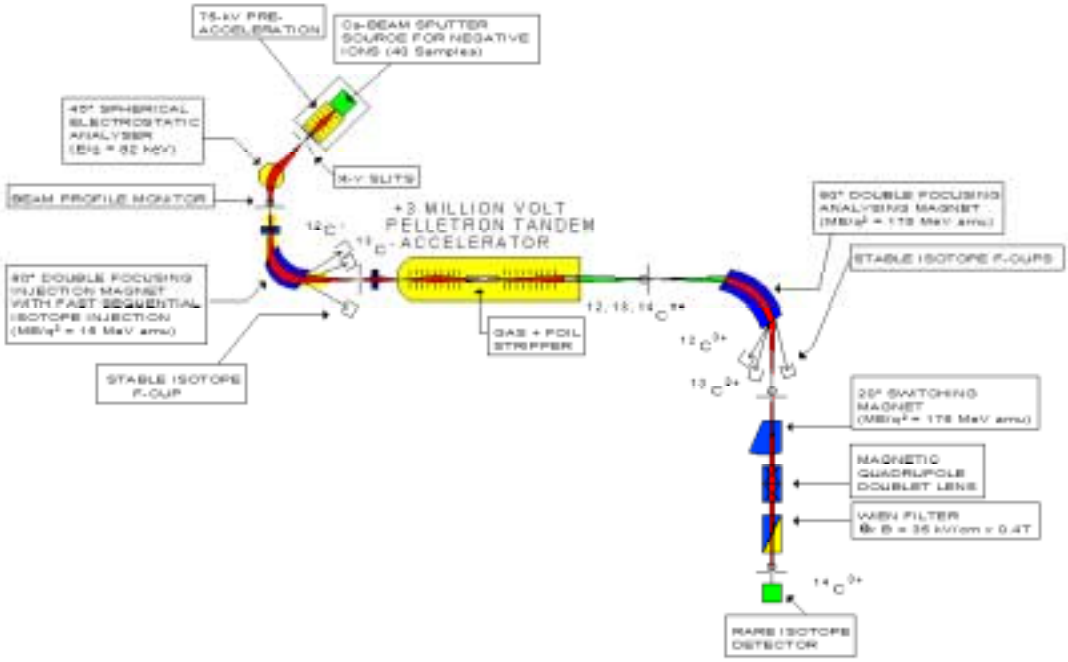

Figure 2.2 A schematic layout of an AMS system (Vienna Environmental Research Accelerator (VERA)). A typical setup for ^{14}C measurement is shown in this figure. (Courtesy of Philippe Collon)

area of the Great Artesian Basin in Australia. In their experiment, the overall system efficiency was 1×10^{-5}. A measurement with a relative precision of 15% required a

sample of 0.5 ml STP krypton gas extracted from 16 tons of groundwater. In a related development [33], Collon *et al*. have detected ^{39}Ar at the isotopic abundance level of

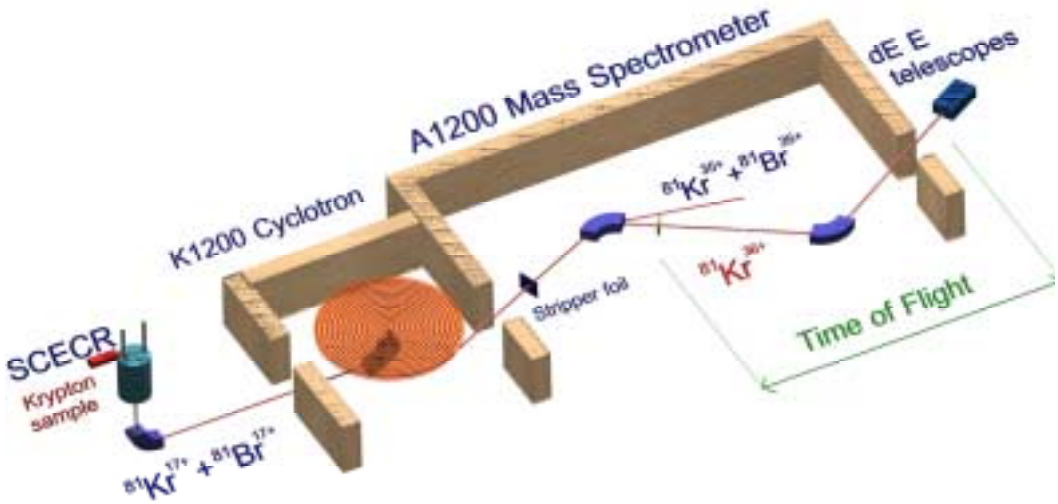

Figure 2.3 Schematic layout of setup at Michigan State University. The superconducting ECR source coupled to the K1200 cyclotron and the A1200 mass spectrometer is used to separate the ^{81}Kr from ^{81}Br by fully stripping at high energy (~4 GeV). After a Be stripper foil, $^{81}Kr^{36+}$ is separated from $^{81}Br^{35+}$. (Courtesy of Philippe Collon)

8×10^{-16} with an efficiency of 1×10^{-3} using ATLAS linear accelerator at Argonne National Laboratory. This method was used to date Atlantic Ocean water samples taken near the South American coast. This collaboration also proposes to analyze ^{85}Kr with the same method [34].

2.3 Existing Laser-based Methods

During the past three decades a number of methods based on laser spectroscopic techniques were proposed and developed. The selectivity achieved by these methods is a result of resonant laser-atom interaction. Atoms of different elements have different resonance frequencies due to their different atomic structures. Atoms of different isotopes of the same element have different isotopic shift due to their variation in nuclear mass, volume, and moments. By tuning the laser frequency to the resonance of a certain isotope, one can selectively excite, ionize, or manipulate the atoms of that isotope while having a much smaller effect on the other isotopes or elements.

The selectivity of an optical excitation is defined as the ratio of the probability of exciting the selected isotope to the probability of exciting the other isotopes or elements. For an atom in the laser beam whose frequency is tuned near the atomic transition, the excitation probability is

$$P \propto \frac{1}{\delta^2 + \frac{\Gamma^2}{4}} \qquad (2.1)$$

where $\delta = \omega_L - \omega_0$ is the laser frequency detuning with ω_L being the laser frequency and ω_0 being the atomic resonance frequency; Γ is the interaction linewidth. When the laser frequency is tuned to the atomic resonance of the selected isotope but away from that of other isotopes or elements, the selectivity can be estimated by

$$s \sim 4 \times \frac{\Delta^2}{\Gamma^2} \text{ when } \Delta >> \Gamma \qquad (2.2)$$

where Δ is the atomic resonance difference between the isotope of interest and the other isotopes or elements.

Take krypton as example, in the case of transition $5s[3/2]_2 \rightarrow 5p[5/2]_3$, Δ is approximately 100 MHz for different isotopes, and Γ is about 6 MHz. The maximum isotopic selectivity for a single excitation is about 1000, which is not sufficient for ultrasensitive trace detection (below 10^{-9}). On the other hand, if we compare krypton with its neighboring element bromine, their atomic resonance differs by $\Delta \sim 1\times10^{15}$ Hz, which yields an extremely high selectivity of 1×10^{17}. In reality, due to the line broadening and non-resonant excitation effects, the actual selectivity is less.

Ultrasensitive trace analysis requires the selectivity of above 10^9 or even higher, which cannot be achieved by only one optical excitation. But consider that an overall selectivity S is the product of the selectivity s_i of each step when multi-step selection processes are applied.

$$S = s_1 \cdot s_2 \cdot ...s_n \qquad (2.3)$$

Based on this principle, the isotopic selectivity can be improved with the following approaches:

(1) laser-based method (with high elemental selectivity) is combined with the mass spectrometry method (with high isotopic selectivity);

(2) multi-step processes of laser excitation can be applied either by cycling in a closed two-level system or successively climbing the steps of multi-step excitation ladder into the continuum.

2.3.1 Resonance Ionization Mass Spectrometry (RIMS)

RIMS combines the sequential optical excitations and mass spectrometry [35]. Single or multi-step resonance excitation and ionization are achieved by irradiation with laser beams, whose frequencies are tuned precisely to the individual atomic transitions of the selected isotope. In most cases, the excitation starts with the ground level, steps up into the intermediate bound states, and ends at ionization potentials. The resulting ions then

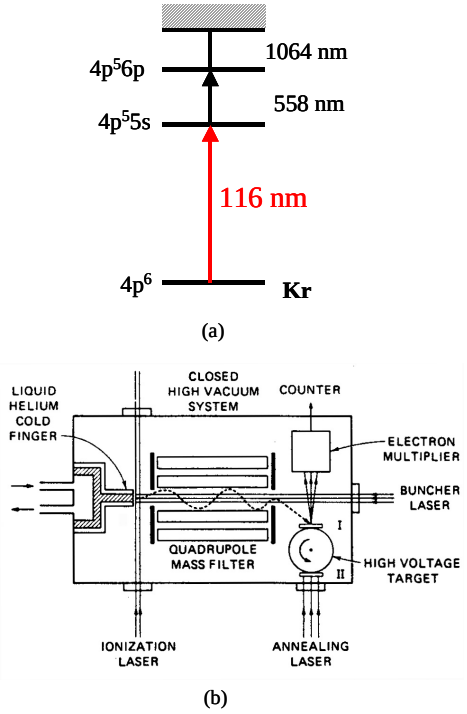

Figure 2.4 Counting ^{81}Kr atoms with RIMS. (a) Atomic energy levels for exciting and ionizing the krypton atoms; (b) A schematic of RIS-TOF system.

pass through a mass filter and are detected by an ion detector such as a channeltron. The combination of isobar selection by resonance ionization and isotope selection by mass spectrometry would, in principle, enable RIMS to reach a selectivity well beyond the

level of 10^{12}. But, in practice, complications such as thermal or collisional ionization limit selectivity.

RIMS was used to count ^{81}Kr atoms in atmospheric and groundwater samples [36, 37, 38]. In the experiment, RIMS has a RIS-TOF (resonance ionization spectrometry - time of flight) system, which had a high element selectivity but a poor isotope selectivity, as shown in Figure 2.4. The krypton sample could only be introduced to RIMS system after it goes through three steps of isotope enrichment in order to increase the initial ratio of ^{81}Kr/Kr from the level of ~10^{-11} up to ~10^{-3}. After the enrichment, the krypton samples were analyzed and ^{81}Kr atoms were detected with the overall system efficiency of ~50%. A typical ^{81}Kr measurement with RIMS needs ~50 liters of groundwater, which is a quite reasonable size of water samples. However, the complicated pre-enrichment work has so far prevented any quantitative measurements.

2.3.2 Photon Burst Mass Spectrometry (PBMS)

Photon-burst method realizes the multi-step optical excitation by exploiting the cycling transition in a two-level system [39]. With a closed two energy levels, a single atom can absorb and emit many photons in a short burst. A fraction of the photons can be detected in coincidence in a short time window and serve as an unambiguous single atom signal. The number of detected photons also represents the number of optical excitations. Therefore the overall selectivity is enhanced exponentially with the number of detected

photons in a single burst. As in the case of RIMS, the selectivity can be further improved

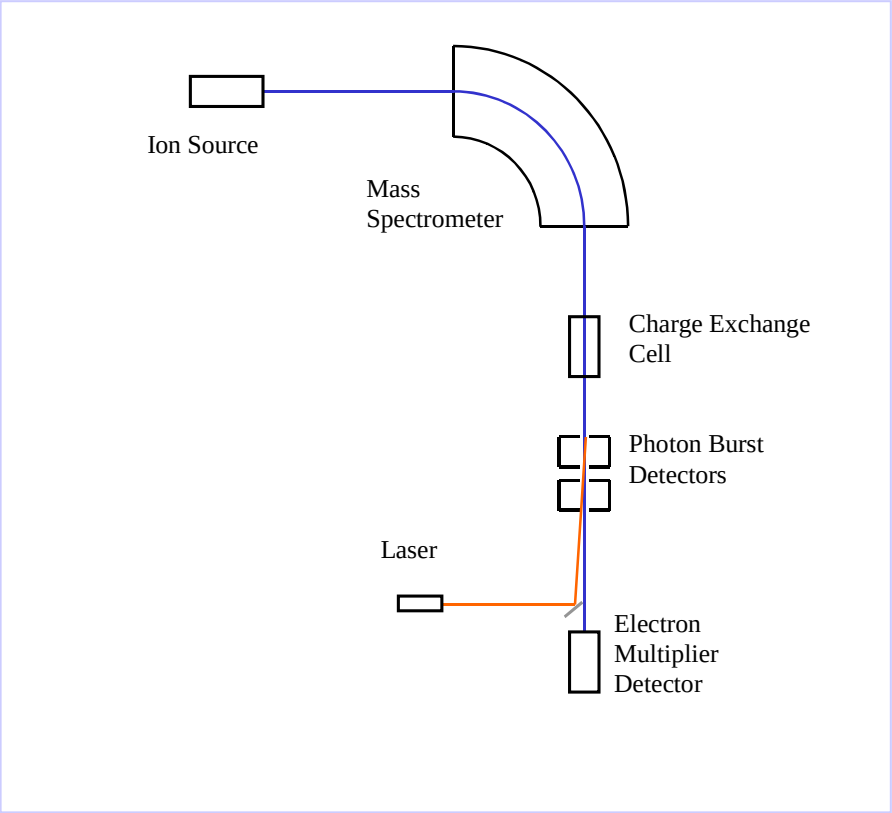

Figure 2.5 Photon Burst Mass Spectrometry. Photon burst is detected when the atom pass through the photon detector region. The photon detector is placed between the magnetic sector and the electron multiplier and would not disturb the normal operation of the machine.

by adding the stage of mass spectrometry to form PBMS, as shown in Figure 2.5.

W. Fairbank Jr. and his coworkers used PBMS method to detect ^{85}Kr atoms at the abundance level of 10^{-9} [40]. In their work, metastable krypton atoms in a fast beam, produced by neutralizing a mass-selected ion beam, are counted when passing through a photon-burst detection region that consists of ten avalanche-photodiode detectors. So far,

the selectivity of this method is still limited by the small number of photons, that can be detected in the interaction time (~μs) as the atoms pass through the laser beam.

2.4 Atom Trap Trace Analysis (ATTA)

ATTA is a relatively new atom-counting method first demonstrated in 1999 [41, 42], and was used to count individual ^{81}Kr and ^{85}Kr atoms at natural isotopic abundance. This method is based on the techniques of laser cooling and trapping developed over the last two decades. In ATTA, an atom of a particular isotope is selectively captured by a magneto-optical trap (MOT) and then detected by observing its fluorescence when it is in the trap. When the laser frequency is tuned to within one or two linewidths on the low-frequency side of the resonance of the isotope of the interest, only the atoms of that selected isotope will be trapped. Atoms of other isotopes are either deflected before reaching the trap or are allowed to pass through the trap quickly without being captured.

A krypton atom can be trapped and observed for 100 ms or longer, during which 10^6 photons are induced from the trapped atom. With the detection efficiency of 2×10^{-3}, 2000 fluorescence photons can be detected in this time period. Remember that each photon is produced in an optical excitation with the selectivity of 10^3, 2000 times of optical excitations therefore yield an impressively high theoretical overall selectivity of 10^{6000}! Furthermore, the viewing region where the atom is trapped and from which the fluorescence is collected is small (sub-millimeter in diameter) so that a spatial filter can be applied to reduce the scattering light from the vacuum chamber walls and the

windows. These advantages provide ATTA with a superb isotopic selectivity as well as a single-atom-level sensitivity. In practice, the selectivity of ATTA is only statistically limited by the atomic beam flux, or, more specifically, by the number of atoms that can be sent through the trap in a reasonable time.

3 Basic Concepts

In this chapter I will review some basic concepts of laser cooling and trapping [43, 44, 45, 46] that are essential for the experiment. Readers who are familiar with this part should skip to the next chapter.

3.1 Light Forces on Atoms

When an atom is irradiated by a laser beam whose frequency is tuned close to a transition frequency of the atom, the atom can absorb a photon and jump from its ground state to an excited state. The atom may return to the ground state by two processes: stimulated emission or spontaneous emission. If the emission is stimulated by the same laser beam, the emitted photon is in the same direction of the absorbed photon and the atom momentum does not change after the absorption-emission cycle. On the other hand, if the emission is spontaneous, photons are emitted in random, symmetrically distributed directions. Repeated absorption followed by spontaneous emissions result in a net momentum change of the atom in the direction of the laser beam.

On average for each cycle of absorption and spontaneous emission, the atom momentum change is

$$\left\langle \Delta \vec{P}_{atom} \right\rangle = \vec{P}_{photon} = \hbar \vec{k}_{photon} \qquad (3.1)$$

where $\vec{k}_{photon}$ is the photon wave vector. For example, a krypton atom can get a velocity change of 6 mm/s due to a single photon kick when the laser frequency is tuned to the $5s[3/2]_2 \rightarrow 5p[5/2]_3$ transition of the krypton atom at 811 nm.

The average force on the atom is given by the average atom momentum change in each cycle divided by the period of an absorption and spontaneous emission cycle, τ_{cycle},

$$\tau_{cycle} = 2\tau_0\left[1+\frac{I_0}{I}\left(1+4\frac{\Delta^2}{\Gamma^2}\right)\right] \qquad (3.2)$$

$$\vec{F} = \frac{\left\langle \Delta\vec{P}_{atom} \right\rangle}{\tau_{cycle}} = \frac{h}{\lambda}\frac{1}{2\tau_0}\frac{\hat{k}}{1+\frac{I_0}{I}\left(1+4\frac{\Delta^2}{\Gamma^2}\right)} \qquad (3.3)$$

where τ_0 is the natural mean lifetime of the excited state; $I_0 \equiv \pi hc/3\lambda^3\tau_0$ is the saturation intensity, which reflects the transition strength; λ is the wavelength of the laser; I is the laser intensity; Δ is the laser frequency detuning, $\Delta = \omega_L - \omega_0$, with ω_L as the laser frequency and ω_0 as the resonance frequency of the transition; and Γ is the linewidth of the excited state, $\Gamma = \frac{1}{\tau_0}$.

Since the force is only due to the process involving spontaneous emissions, it is often called the spontaneous force. Sometimes it is also referred to as the radiation force or

scattering force. At high laser intensity I, the force saturates to $\frac{h}{\lambda}\frac{1}{2\tau_0}$, which is limited by how rapidly the spontaneous emission can occur. The resulting acceleration of the atom is significant. For krypton atoms with λ=811nm, the maximum acceleration is 1×10^5 m/s^2, which is 10^4 times larger than the acceleration of gravity on the surface of the earth. This enormous acceleration can stop a krypton atom with an initial speed of 300 m/s in 3 ms over 50 cm.

Approximately 5×10^4 cycles of absorption-spontaneous emission processes are needed to bring a krypton atom to rest. However, in reality, two phenomena can interrupt this scattering process. One is optical pumping, the other is changing Doppler shift [45, 46].

In a transition of multilevel atoms, the ground level is usually not a single state, but multiple states split due to hyperfine interaction. The split in transition frequency can be as much as hundreds times the natural linewidth of the excited states. An atom excited by the laser beam from one of the hyperfine ground states to an excited state may decay by spontaneous emission to another hyperfine ground state. This process is called ``Optical pumping". The optical pumping problem can be understood by referring to Figure 3.1, which shows the atomic energy level relevant to trapping ^{83}Kr. Consider a laser that is tuned to be resonant with the $F=13/2\rightarrow F'=15/2$ transition, it is also possible to excite the atom to the neighboring $F'=13/2$ or $F'=11/2$ level, from which the atom can decay to $F=11/2$ or $F=9/2$ level. Since the transition from these "wrong" levels

is out of the resonance with the laser, no further absorption will occur and the scattering process stops. One solution to the problem of optical pumping is to add an additional

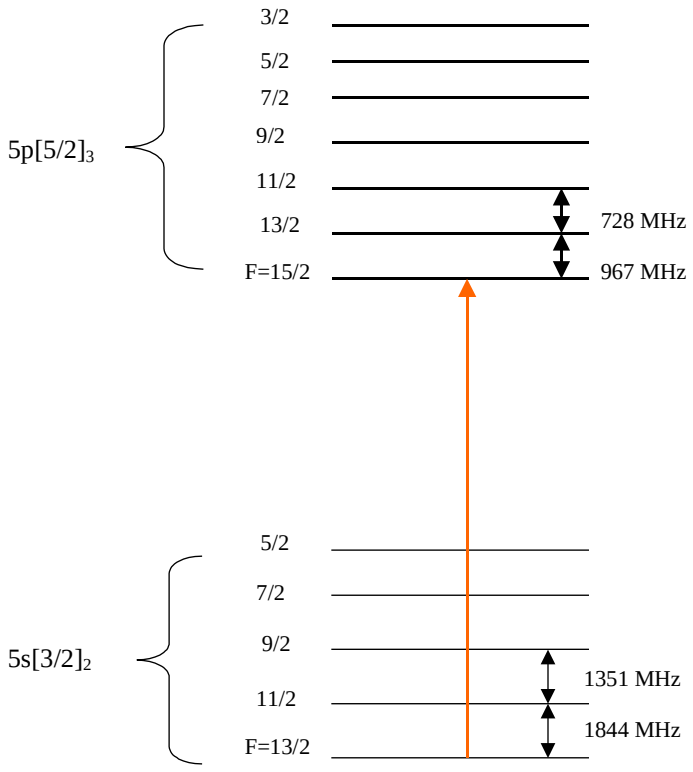

Figure 3.1 ^{83}Kr atomic energy level (relevant to trapping and no scale).

laser, tuned to the resonance between the "wrong" hyperfine ground state and the excited state ($F = 11/2 \rightarrow F' = 13/2$ and $F = 9/2 \rightarrow F' = 11/2$). This second laser frequency is called "sideband" or "repumping" frequency. The repumper laser can keep the atoms out of the ``wrong" ground state.

When the Doppler effect is considered, Δ in Eq. (1.1) has to be changed to Δ-kυ. When the velocity of the atom is in the opposite direction of the laser beam, $-k\upsilon$ is positive; when in the same direction, $-k\upsilon$ is negative. When the laser intensity I is not much larger than saturation intensity I_0, the spontaneous force can be large only if $(\Delta - k\upsilon) \sim \Gamma$, which can be realized by tuning the laser frequency to meet the requirement with atoms of a particular velocity. But as the atom is slowed down, it will go out of the resonance due to the changing Doppler effect. For krypton atoms, 700 cycles of absorption-emission process will change the velocity by 4.2 m/s, which corresponds to a Doppler shift of $2\pi \times 5$ MHz, comparable to the natural linewidth of the excited state ($2\pi \times 5.3$ MHz). If we assume the laser intensity I is equal to saturation intensity I_0, the acceleration will be reduced by a factor of 3 after 700 cycles, or about one percent of the scattering processes required to bring the atom to rest. The solutions to solve the problem of "changing Doppler shift" will be discussed in the following sections.

3.2 Transverse Cooling

Consider the case of the atoms interacting with two opposing laser beams. In the experiment, this method is used to "transversely cool" the atomic beam in order to reduce the divergence of the beam and to increase the beam flux in the forward direction. Based on a simple model of optical molasses, one can derive the Doppler-cooling limit, which is

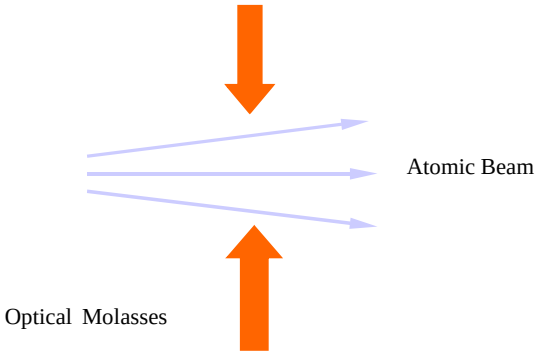

(a)

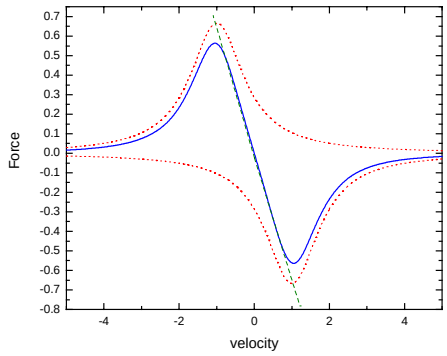

(b)

Figure 3.2 **(a)** Schematic of one-dimensional optical molasses; **(b)** Velocity dependence of the optical damping forces for one-dimensional optical molasses. The two dotted traces show the force from each beam, and the solid curve is their sum. These are calculated for $I / I_0 = 2$ and $\Delta = -\Gamma$.

the theoretical limit on the lowest temperature of the atomic ensemble with this type of cooling.

When the intensity of each laser beam is small, i.e. $\frac{I}{I_0} << 1$, one can assume that the total force on the atom is the sum of the radiation pressure from each of them,

$$F = \frac{\hbar k\Gamma}{2}\frac{\frac{I}{I_0}}{1+\frac{I}{I_0}+\left[\frac{2(\Delta - k\upsilon)}{\Gamma}\right]^2} - \frac{\hbar k\Gamma}{2}\frac{\frac{I}{I_0}}{1+\frac{I}{I_0}+\left[\frac{2(\Delta + k\upsilon)}{\Gamma}\right]^2} \qquad (3.4)$$

In the approximation that $|k\upsilon| << \Delta$, we have

$$F = 4\hbar k\frac{I}{I_0}\frac{2\Delta}{\Gamma}\frac{k\upsilon}{\left(1+\frac{4\Delta^2}{\Gamma^2}\right)^2} = -\alpha\upsilon \qquad (3.5)$$

For $\Delta < 0$, this force is a friction force, linear in and opposing υ. Figure 3.2(a) shows the schematic of one-dimensional optical molasses; Figure 3.2(b) shows velocity dependence of the optical damping forces for one-dimensional optical molasses. When the velocity is small ($< \Gamma / k$), the force is proportional to the velocity ($-\alpha\upsilon$), shown as the straight dashed line in the figure.

The damping force cools the atoms at the rate of $\left(\frac{dE}{dt}\right)_{cool} = -\alpha\upsilon^2$. While the radiation pressure that produces the damping force results from discrete transfers of momentum when atoms absorb or spontaneously emit photons, this discreteness will lead to the random diffusion force which can heat the atoms. Each absorption process induces a random walk with a momentum step size $\hbar k$, with equal possibility of being positive or negative. In the same way, each spontaneous emission represents a random-walk step of $\hbar k$. After a given number N of steps, the mean square momentum of the atom will be $2N\hbar^2k^2$. Given the photon scattering rate R, we can get the heating rate of the atom,

$$\left(\frac{dE}{dt}\right)_{heat} = \frac{1}{2M}\frac{dP^2}{dt} = \frac{\hbar^2 k^2}{M} R \qquad (3.6)$$

where $R = \frac{\Gamma}{2}\frac{2\frac{I}{I_0}}{1+\frac{I}{I_0}+\frac{4\Delta^2}{\Gamma^2}}$ is the sum of photon scattering rate from each of the two beams.

At equilibrium, $\left(\frac{dE}{dt}\right)_{cool} = \left(\frac{dE}{dt}\right)_{heat}$, we obtain $\upsilon^2 = \frac{\hbar\Gamma}{4M}\left(\frac{\Gamma}{2|\Delta|}+\frac{2|\Delta|}{\Gamma}\right)$. Taking the thermal energy to be $\frac{1}{2}k_B T = \frac{1}{2}M\upsilon^2$, we have

$$k_B T = \frac{\hbar\Gamma}{4}\left(\frac{\Gamma}{2|\Delta|}+\frac{2|\Delta|}{\Gamma}\right) \qquad (3.7)$$

When $\Delta = -\frac{1}{2}\Gamma$, the temperature has a minimum value, $k_B T_{\min} = \frac{1}{2}\hbar\Gamma$. This is so called "Doppler Limit". For krypton, with $\Gamma = 2\pi\times 5.3$ MHz, the Doppler Limit is 130 μK, corresponding to the speed of 0.2 m/s.

3.3 Deceleration of an Atomic Beam

Slowing down an atomic beam can be achieved by directing a laser beam opposite to the atomic beam. As discussed earlier, when the atoms slow down, changing Doppler shift moves them out of resonance with the interacting laser beam, thereby limiting the

cooling to a few linewidths. In order to accomplish deceleration which can change the atomic velocity by 10^2 m/s, it is necessary to maintain $\Delta - k\upsilon \sim \Gamma$, where $\Delta = \omega_L - \omega_a$ throughout the deceleration process. This can be done by changing ω_L or ω_a to compensate for the changing Doppler shift. The two well-developed methods are the "chirping" method and the "Zeeman slowing" method.

In the chirping method [47], the laser frequency is swept upward to compensate the decreasing Doppler shift as the atoms slow down. There is an upper limit on the laser frequency sweeping rate, which is determined by the maximum acceleration,

$$\frac{d\omega_L}{dt} = ka \le ka_{\max} \qquad (3.8)$$

where a is deceleration and $a_{\max} = \frac{1}{2}\frac{\hbar k\Gamma}{M}$.

The chirping method produces pulses of slow atomic beam. Atoms with various initial longitudinal velocities are slowed down to the same final velocity at the same time but at different locations along the atomic beam.

In the Zeeman-slowing method [48], a spatially varying magnetic field is applied to tune the atomic energy level to compensate for the changing Doppler shift,

$$\mu' B(z) = \hbar k \upsilon(z) \qquad (3.9)$$

where $\mu' \equiv \left(g_e m_e - g_g m_g\right)\mu_B$, subscript g and e refer to ground and excited states, $g_{g,\,e}$ is the Lande g-factor, μ_B is the Bohr magneton, and $m_{g,\,e}$ is the magnetic quantum

number. For uniform deceleration $a \equiv \eta a_{\max}$ from initial velocity υ_0, the magnetic field spatial profile is

$$B(z) = \frac{\hbar k \upsilon_0}{\mu'} \sqrt{1 - \frac{\eta \hbar k \Gamma}{M {\upsilon_0}^2} z} = B_0 \sqrt{1 - \frac{z}{z_0}} \qquad (3.10)$$

where $B_0 \equiv \frac{\hbar k \upsilon_0}{\mu'}$, $z_0 \equiv \frac{M {\upsilon_0}^2}{\eta \hbar k \Gamma}$. Similar to the chirping method, there is a maximum magnetic field gradient determined by the maximum deceleration,

$$\left(\frac{\mu'}{\hbar k} \right)^2 B(z) \left(\frac{dB(z)}{dz} \right)_{\max} = a_{\max} \qquad (3.11)$$

Compared with the chirping method, Zeeman-slowing method can generate a continuous slow atomic beam. Atoms with different initial velocities are slowed down to the same velocity at the same place.

3.4 Magneto-Optical Traps

The basic principle of Magneto-Optical Trap (MOT) [49] can be explained by considering a simple atom with two levels, a $J_g = 0$ ground level and a $J_e = 1$ excited state, shown in Figure 3.3. In a weak inhomogeneous magnetic field $B(z) = bz$, the excited state is split into three energy levels, due to Zeeman effect. The magnetic field is gnerated by a pair of anti-Helmholtz coils. Two counterpropagating laser beams of

opposite circular polarization, each detuned below the zero field atomic resonance, are incident on atoms.

Consider an atom at $+z_0$. The energy level $J_e = 1,\ m_J = -1$ is shifted down so that the

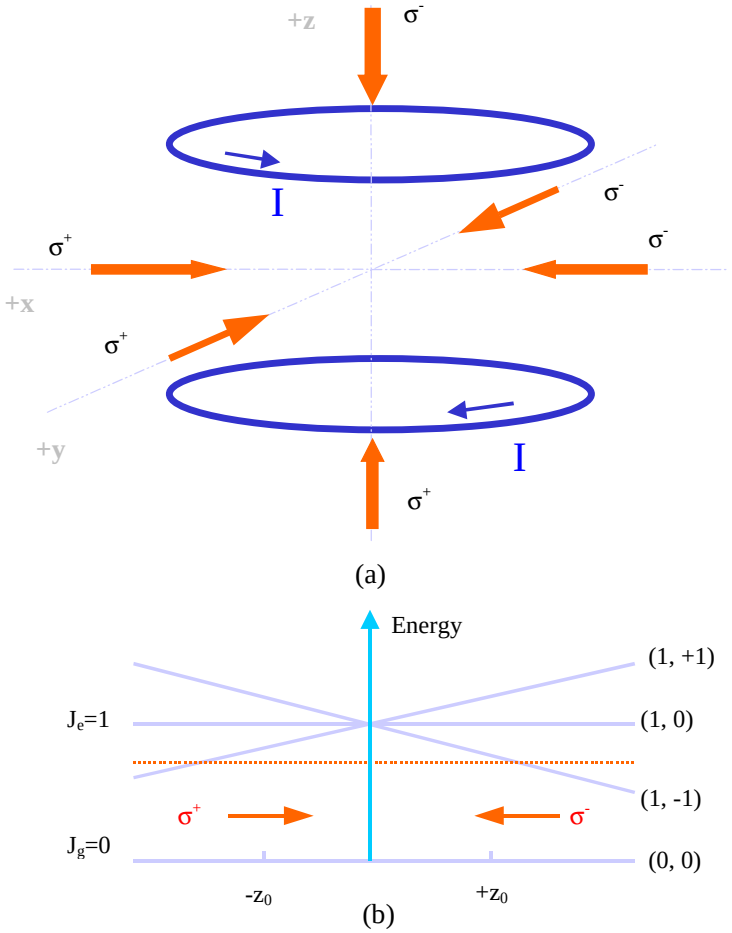

Figure 3.3 (a) Schematic of three-dimensional trapping. The quadrupole field is generated by two anti-Helmholtz coils; (b) One dimensional MOT arrangement with a two-level atomic energy diagram.

transition of $J_g \rightarrow J_e, m_J = -1$ is on resonance with the laser frequency. However, the

transition of $J_g \rightarrow J_e, m_J = +1$ is out of resonance with the laser frequency. As a result, the atom will absorb more σ^- photons than σ^+ photons, and the atom is pushed toward the origin. For an atom at $-z_0$, the Zeeman shift is reversed, and the atom will again be pushed toward to the origin.

Tuning the laser frequency below the atomic resonance also provides damping, as discussed in "Optical Molasses". Therefore, confining and cooling of the atoms are accomplished simultaneously in a MOT.

When we consider a scattering force in a MOT, the term $(\Delta - k\upsilon)$ needs to be replaced by $(\Delta - k\upsilon - \frac{\mu' G}{\hbar} z)$, where $\Delta = \omega_L - \omega_0$, ω_0 is the atomic transition without external magnetic field and G is the magnetic field gradient. In the approximation of low laser intensity, the total force is again given by the sum of the two radiation pressure from each of the two beams and can be expressed as

$$F = -\alpha\upsilon - \kappa z \qquad (3.12)$$

where α is the same as in "optical molasses"; $\kappa = \frac{|\mu'| G}{\hbar k} \alpha$.

The size of the atomic cloud can be derived from the temperature of the MOT,

$$\frac{1}{2}\kappa z^2 = \frac{1}{2} k_B T \qquad (3.13)$$

For a temperature of the Doppler Limit, the size of the MOT is in sub-millimeter range.

4 Laser Cooling and Trapping of Metastable Krypton Atoms

4.1 Relative Krypton Atomic Transitions

Krypton gas constitutes 1 ppm (parts per million) of the earth's atmosphere in fractional volume. It has six stable isotopes, ^{78}Kr (isotopic abundance = 0.35%), ^{80}Kr (2.25%), ^{82}Kr (11.6%), ^{83}Kr (11.5%), ^{84}Kr (57%), ^{86}Kr (17.3%), and two long-lived radioactive isotopes, ^{85}Kr (isotopic abundance is 2×10^{-11}) and ^{81}Kr (isotopic abundance is 5×10^{-13}). The even isotopes have no nuclear spin. Among the odd isotopes, ^{83}Kr and ^{85}Kr have nuclear spin $I = 9/2$, ^{81}Kr has nuclear spin $I = 7/2$.

A neutral krypton atom has 36 electrons. In the ground state, all shells are closed ($1s^2 2s^2 2p^6 3s^2 3p^6 4s^2 3d^{10} 4p^6$) and the configuration is $4p^6(^1S_0)$. Excited states are formed by excitation of a valance electron from the outmost shell, which will not be closed and therefore possesses both orbital angular momentum ($\vec{L}$) and spin angular momentum ($\vec{S}$). Together with the orbital angular momentum ($\vec{l}$) and spin angular momentum ($\vec{s}$) of the outer electron, these are coupled to form a total angular momentum of the atom,

$$\begin{aligned} \vec{j} &= \vec{L} + \vec{S}, \\ \vec{K} &= \vec{j} + \vec{l}, \\ \vec{J} &= \vec{K} + \vec{s} \end{aligned} \qquad (4.1)$$

and the notation of the metastable level of the atom is ${}^{2S+1}L_j nl[K]_J$, where n is the outer electron's principal quantum number.

Figure 4.1 shows the atomic level diagrams of krypton. The excitation of the first allowed transition from the ground-level $4p^6(^1S_0)$ to an intermediate level $5s[3/2]_1$, requires VUV photons at wavelength of 124nm. A MOT based on this transition is impossible with present laser technology as CW lasers of this wavelength are far from having sufficient power needed for trapping. On the other hand, Kr atoms can be excited

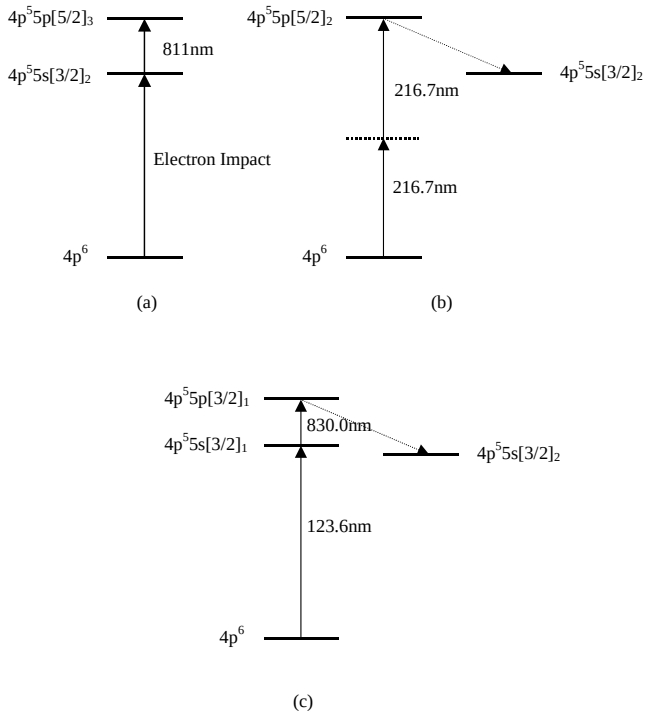

Figure 4.1 Krypton energy level diagrams. (a) Excitation scheme used in the laser trapping of Kr^* atoms; (b) Populating the metastable level via a non-resonant UV+UV excitation; (c) Populating the metastable level via a resonant VUV+IR excitation.

from the ground-level to the metastable level $5s[3/2]_2$ (lifetime ~ 40 s) via electron-impact or photon excitations, and laser trapping and cooling of Kr* (metastable Kr) atoms based on the transition $5s[3/2]_2 \rightarrow 5p[3/2]_3$ have been realized with the laser with wavelength of 811nm. Note that the selection rules that slow down the decay of metastable Kr atoms break down easily upon collisions of the metastable Kr atoms with Kr atoms (in the ground-level and in excited states), other atoms, molecules, or surface. This characteristic makes Kr* atoms fragile and difficult to produce. On the other hand, lack of a background of Kr* vapor makes the individual trapped atoms easier to detect.

For even isotopes, the transition $5s[3/2]_2 \rightarrow 5p[3/2]_3$ is "closed", i.e. the excited atoms will decay back to the lower states from where it will be re-excited by the laser light. For odd isotopes (^{83}Kr, ^{85}Kr and ^{81}Kr), metastable level $5s[3/2]_2$ and upper level $5p[5/2]_3$ split to numerous energy levels due to hyperfine interaction. The hyperfine structure of the odd isotopes is shown in Figure 4.2. For ^{83}Kr and ^{85}Kr, we use the transition $F = 13/2 \rightarrow F' = 15/2$ to cool and trap the atoms (for ^{81}Kr, $F = 11/2 \rightarrow F' = 13/2$). In practice, those transitions are not perfectly "closed". It is possible that, for ^{83}Kr and ^{85}Kr, the atoms will be excited to the neighboring upper states F' =13/2 or F'=11/2 (for ^{81}Kr, F'=11/2 or F'=9/2) and then decay back to F=11/2 or F=9/2 (for ^{81}Kr, F=9/2 or F=7/2) so that the atoms will no longer interact with the laser light tuned to the resonance of $F = 13/2 \rightarrow F' = 15/2$ (for ^{81}Kr, $F = 11/2 \rightarrow F' = 13/2$). Those atoms will become "dark" to the laser light.

The transition rate *R* can be calculated by

$$R = 1/\tau = \frac{1}{2\tau_0}\left[1+\frac{I_0}{I}\left(1+4\frac{\Delta^2}{\Gamma^2}\right)\right]^{-1} \qquad (4.2)$$

where the definitions of τ_0, I_0, I, Δ, Γ are the same as in Chapter 3 (see equation 3.3). Using this equation, we can calculate the trapping transition rate and the optical pumping

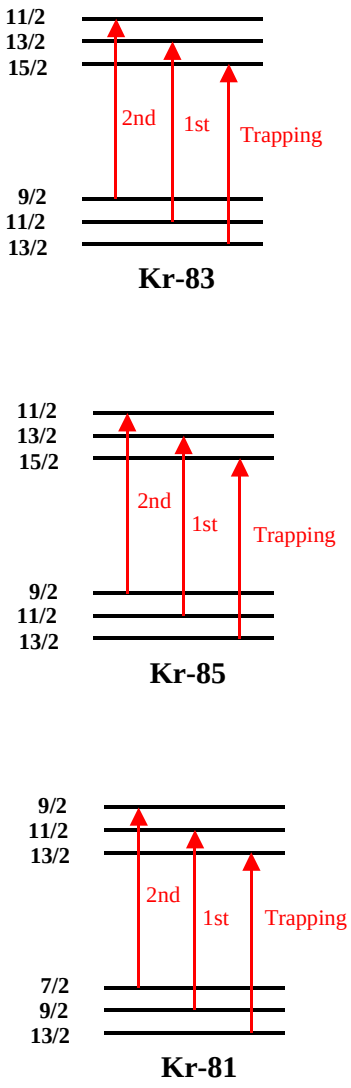

Figure 4.2 Hyperfine structures of the odd krypton isotopes. Note that only the levels relevant to trapping are drawn.

transition rates, therefore derive the leak rate (i.e. how fast the atom will leak to the dark

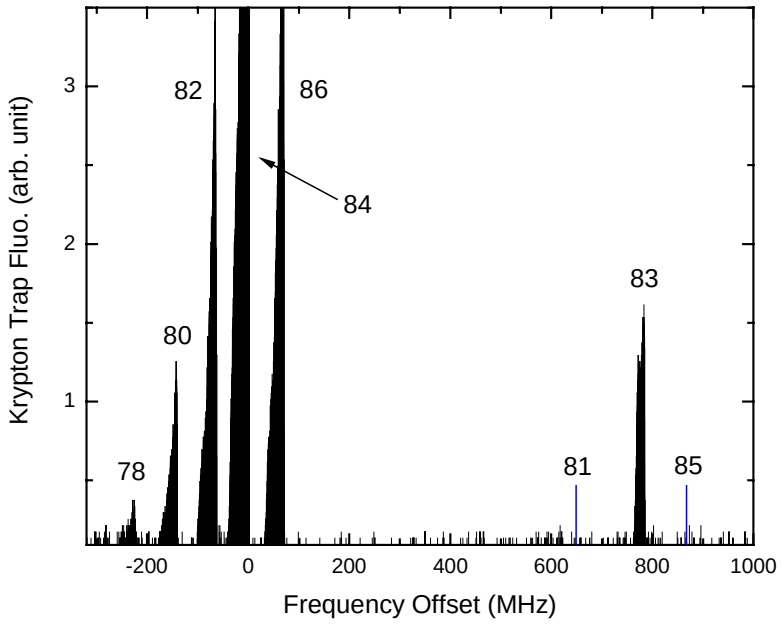

Figure 4.3 Fluorescence of trapped krypton atoms. Dark bands are the signals of stable isotopes measured with a low gain pin photo-diode detector. Line markers mark the frequency positions of the two rare isotopes.

state). Take ^{83}Kr as example, when the interacting laser beam intensity is 10 mW/cm^2 and is 6 MHz red-detuned to the trapping transition frequency, the trapping transition rate is $1.3\times10^7/s$, the transition rate to $F'=13/2$ is $3.6\times10^3/s$, and the transition rate to $F'=11/2$ is $1.2\times10^3/s$. Therefore, the atom will be pumped to $F=11/2$ approximately every 10^{-4} seconds; the atom will be pumped to $F=9/2$ approximately every 10^{-3} seconds.

To pump the atoms out of those "dark" lower states, a laser light with "sideband" frequencies (for ^{83}Kr and ^{85}Kr, $F = 11/2 \rightarrow F' = 13/2$ and $F = 9/2 \rightarrow F' = 11/2$; for ^{81}Kr, $F = 9/2 \rightarrow F' = 11/2$ and $F = 7/2 \rightarrow F' = 9/2$) is needed. The sideband is essential to trap the odd isotopes of krypton at a high loading rate and to increase the lifetime of atoms in the trap. Take ^{83}Kr as an example, we applied 2% of the total laser power to the first sideband and 0.5% of the laser power to the second sideband to reduce the time that the atom spends in the dark states to shorter than 1 μs.

Atoms of different isotopes have different isotopic shifts due to their variations in the

Table 4.1 Krypton Isotopic shifts on $5s[3/2]_2 \rightarrow 5p[5/2]_3$ transition (for odd isotopes, only transitions relative to trapping are listed)

Isotope	Hyperfine	Trapping/sidebands	Calculation	Measurement
81	$7/2 \rightarrow 9/2$	2nd sideband	-800	-795.9
83	$9/2 \rightarrow 11/2$	2nd sideband	-706	-711.8
85	$9/2 \rightarrow 11/2$	2nd sideband	-688	-687.2
81	$9/2 \rightarrow 11/2$	1st sideband	-309	-308.5
78			-217	
80			-138	
83	$11/2 \rightarrow 13/2$	1st sideband	-87	-88.9
85	$11/2 \rightarrow 13/2$	1st sideband	-77	-76.4
82			-64	
84			0	
86			66	
81	$11/2 \rightarrow 13/2$	trapping	656	651.8
83	$13/2 \rightarrow 15/2$	trapping	783	786.9
85	$13/2 \rightarrow 15/2$	trapping	870	868.7

nuclear mass, volume and moments. When the laser frequency is tuned to the resonance of the isotope of interest, only atoms of that particular isotope are trapped. Figure 4.3 shows the fluorescence signals of trapped Kr* atoms when the laser frequency is scanned through the resonance of different krypton isotopes. The frequency positions of rare isotopes are also marked in the figure. For both stable and radioactive krypton isotopes, the isotopic shifts of $5s[3/2]_2 \rightarrow 5p[5/2]_3$ have been calculated [50]. For rare krypton isotopes (^{85}Kr and ^{81}Kr), the isotopic shifts of $5s[3/2]_2 \rightarrow 5p[5/2]_3$ have been measured [51]. For ^{85}Kr measurement, a high-activity gas was separated from nuclear fission products; for ^{81}Kr measurement, a sample of ^{81}Kr was produced in a reactor by neutron activation on enriched ^{80}Kr. The previous results on the isotopic shifts are listed in Table 4.1.

4.2 Laser System for Trapping Krypton Atoms

The all-diode-laser system is shown in Figure 4.4. The system supplies laser beams for transverse cooling, slowing, and trapping of metastable krypton atoms.

In the system, there are three diode lasers and one tapered amplifier. The three diode lasers are one SDL-5401 (serves as Master Laser) and two SDL 5422 (serve as Slave Lasers). The tapered amplifier (TA) is Toptica TA-0810. For each of the lasers or the tapered amplifier, its wavelength and mode are monitored by a wavemeter (Buleigh WA 20) and a spectrum analyzer (1.5 GHz free spectral range).

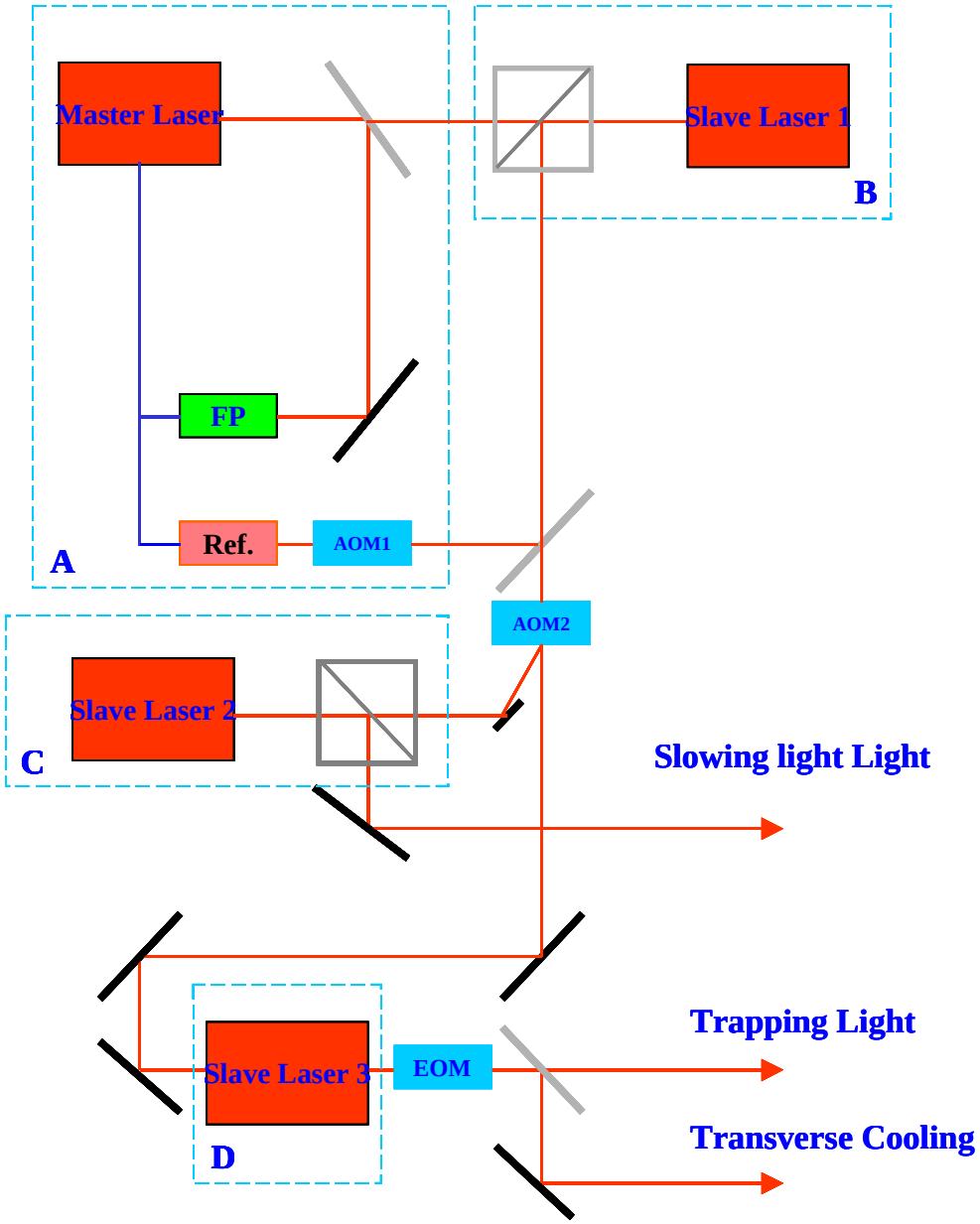

Figure 4.4 Schematic of laser setup for trapping Kr* atoms.

The Master Laser (SDL-5401) is an extended-cavity diode laser (ECDL) [52]

employing a diffraction grating. Its output is 12 mW. The laser frequency is electronically locked [53] onto a Fabry-Perot interferometer through current feedback loop and piezoelectric transducer (PZT) feedback loop. The short-term linewidth is about 1 MHz.

Slave Laser 1 (SDL-5422) is injection-locked [53, 54] to the Master Laser, as shown in Figure 4.4. The output is greater than 100 mW, of which 25 mW is sent to the krypton reference cell (500 mTorr krypton gas sealed inside) for the saturation absorption spectroscopy [55]. The light double-passes through an acousto-optic modulator (AOM 1, Brimrose TEF-380-200-.811, bandwidth 200 MHz) so that the light frequency is red-shifted by about 800 MHz. The saturation absorption signal is sent into a lock-in amplifier. Lock-in detection takes the derivative of the saturation absorption lineshapes and its output signal is used as an error signal to lock the Fabry-Perot interferometer to the ^{84}Kr ($5s[3/2]_2 \rightarrow 5p[5/2]_3$) transition through the Fabry-Perot PZT feedback loop. In this way, the master laser frequency, after about 800 MHz redshift, is locked onto the ^{84}Kr transition line.

The rest 75-mW laser power of Slave Laser 1 is used to injection-lock Slave Laser 2 and the tapered amplifier. The light passes through AOM 2 (Brimrose, TEF-350-50-.811). The zeroth order (45 mW) is sent into the tapered amplifier. The first order (5 mW and red-shifted by 360 MHz) is sent into Slave Laser 2.

100 mW output of Slave Laser 2 is red-shifted by 360 MHz to the trapping light and used as the slowing light. Before the light goes to the trap, we expand the beam and trim

the edge of the beam in order to obtain a uniform beam spatial profile. The intensity of the slowing light is 5 mW/cm^2.

The tapered amplifier has an output of 500 mW with the injection laser power of 40 mW. The fluctuation in its output is less than one percent. Long-term (10-hour) decrease in the laser power is less than 5%. The output of the tapered amplifier is the source of trapping light and transverse cooling light.

The two sidebands needed for repumping transitions are generated by sending the output of the tapered amplifier through a tunable traveling-wave electro-optic modulator (EOM, Quantum Technology, TWAP-11, up to 1.6 GHz) [56]. The modulation frequency for 1^{st} sideband and 2^{nd} sideband are about 900 MHz and 1.5 GHz, respectively.

The 900-MHz frequency is generated by a voltage controlled oscillator (VCO, MiniCircuits, ZOS-1025, up to 1 GHz). The 1.5-GHz frequency is generated by another VCO (MiniCircuits, ZOS-1025) along with a frequency doubler (MiniCircuits, ZFL-2500, up to 2.5 GHz) and an amplifier (MiniCircuits, ZFL-2500, up to 2.5 GHz). The two RF signals are combined by a power combiner (MiniCircuits, ZESC-2-11, frequency range between 10 MHz and 2000 MHz) and sent into an RF amplifier (Amplifier Research, 5S1G4). For the frequency of 900 MHz, the input is about -2 dBm and the output is about 34 dBm; for 1.5 GHz, the input is -5 dBm and the output is about 28 dBm.

The output of the amplifier is sent into the EOM, which then generates the 900-MHz sideband with 2 percent of the total laser power and the 1.5-GHz sideband with 0.3 percent of the total laser power.

After laser beam passes through the EOM, the total laser power is 400 mW, 40 percent of which is used for transverse cooling, the remaining 60 percent is used for trapping. Note that the sidebands are not added to the slowing light in order to avoid the possibility of exciting any unintended transitions inside the Zeeman slower, where the hyperfine structure is further complicated due to Zeeman shifts.

4.3 Making of Metastable Krypton Atomic Beam

The metastable krypton atomic beam is produced by a rf-driven discharge (Figure 4.5). The discharge is driven by a rf resonator which consists of a copper coil enclosed in a brass shield. From the upstream chamber (source chamber) to the downstream chamber (transverse cooling chamber), krypton gas flows through a glass tube, in which a plasma is produced by rf power coupled in from the surrounding coil. In this discharge region, the atoms are excited from the ground state to the metastable level $5s[3/2]_2$ via collisions with energetic electrons and ions.

In order to run the discharge in a good condition, several parameters have to be well chosen. First, rf frequency is very critical for operating the discharge. Different rf resonator may have different rf resonance frequency due to variations in coil geometry. The resonance frequency needs to be carefully searched through the range from a few

tens of MHz up to a few hundred MHz. Several resonance frequencies may exist for one resonator and line-width for each resonance frequency is approximately 10 MHz. For instance, in our experimental setup, we can drive the discharge at 70 MHz and 230 MHz. We found that the metastable beam flux at 230 MHz was two times that at 70 MHz when other conditions are the same. Second, it is usually true that more rf power produces higher metastable beam flux. But we found that higher metastable beam flux did not always lead to higher trap loading rate. This may be due to the collisions between the trapped atoms with more energetic ions or atoms in the trap chamber. It is also possible that the intense discharge produces higher-temperature metastable krypton atoms, which are difficult to be slowed down and captured. Thirdly, pressures both in upstream chamber and downstream chamber need to be optimized. Note that a high pressure (>10 mTorr in the upstream chamber or $>1\times10^{-4}$ Torr in the downstream chamber) will dramatically quench the metastable atoms. Finally, when a glass tube of the discharge is put into the vacuum for the first time, turning on the discharge will produce a significant amount of hydrogen and water. Flushing the glass tube with the discharge on for a certain time period (~10 hours) before operation is necessary. How long to flush largely depends on the humidity of location where the glass tube is stored. Usually long-time storage in a humid environment will need extended flushing until the pressures of water and hydrogen drop well below the operation pressure of krypton.

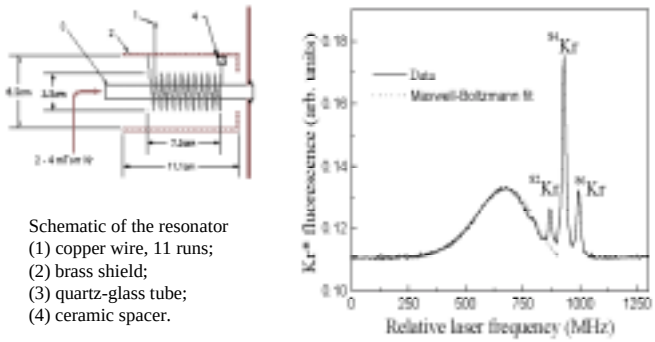

Figure 4.5 (a) Schematic of RF resonator. Note that the ceramic spacer is used to isolate that end of coil from the shield. **(b)** Kr^* beam Fluorescence vs. laser isotopes.

Laser spectroscopy techniques are used to measure the beam flux and the velocity distribution (shown in Figure 4.5 (b)) [57]. The optimum metastable krypton beam flux is achieved when the pressure is about 4 mTorr in the source chamber (shown in Figure 4.6) and 2×10^{-5} Torr in the transverse cooling chamber (shown in Figure 4.6). Under these conditions, we can produce a beam of metastable krypton atoms with an angular flux density of 4×10^{14} $s^{-1}sr^{-1}$, with Kr^*/Kr ratio of 10^{-3} and the most probable velocity of 300 m/s.

4.4 Trapping of Metastable Krypton Atoms

The krypton gas sample is injected into the vacuum system from a reservoir. In the discharge region, a fraction of krypton atoms (about 10^{-3}) are excited into the metastable level. After exiting the discharge region, those atoms remain in the metastable level until

they hit the vacuum chamber walls. Two-dimensional transverse cooling light is applied to reduce the metastable atomic beam divergence and amplify the beam flux in the forward direction. The thermal metastable krypton atoms are then decelerated through the "Zeeman slower" region and loaded into the magneto-optical trap (MOT).

4.4.1 Vacuum System

The vacuum system is shown in Figure 4.6. The krypton gas sample is first loaded from a sample container into the reservoir. The reservoir has a volume of 475 ml. A Baratron gauge (MKS 722A, full pressure range is 1 Torr, the resolution is 0.5 mTorr) is used to measure the gas pressure in the reservoir, from which we derive the initial amount of gas in the sample as well as the gas consumption rate during the measurement.

The gas sample is injected through a fine leak valve into the source chamber. A getter pump (SAES, GP 50, pumping speed 100 l/s for nitrogen) in the source chamber is used to remove the reactive gases such as hydrogen, water, etc., while leaving the noble gases, including krypton sample, intact. The source chamber has a volume of 5 liters and the

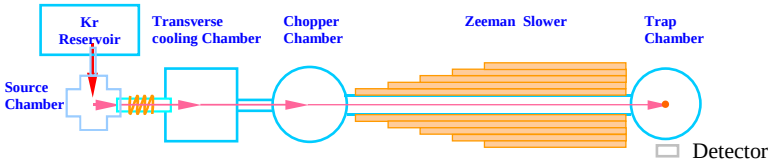

Figure 4.6 Schematic of krypton atomic beamline.

pressure is maintained at 4 mTorr throughout the experiment. Pressure in the source chamber is monitored using a convectron gauge.

The source chamber and the transverse cooling chamber are connected with the glass tube (18 cm long, 1 cm in diameter) of the rf-discharge source.

In the transverse cooling chamber, the pressure is 2×10^{-5} Torr in the experiment. This chamber is pumped by an oil-free, magnetically coupled turbo pump (LEYBOLD, TurboVac 340M, pumping speed 270 l/s for nitrogen).

Between the transverse cooling chamber and the chopper chamber is a collimator (12.5 cm long, 1.6 cm in diameter) which is used to reduce the conductance between the chambers.

Another turbo pump (LEYBOLD, TurboVac 151, pumping speed 150 l/s for nitrogen) is used to pump the chopper chamber, which has a vacuum of 4×10^{-7} Torr in the

Table 4.2 Vacuum system parameters.

	Pressure (Torr)	Pump
Source chamber	4×10^{-3}	Getter Pump (SAES, GP 50)
Transverse Cooling Chamber	2×10^{-5}	Turbo Pump (LEYBOLD, TurboVac)
Chopper chamber	4×10^{-7}	Turbo Pump (LEYBOLD, TurboVac)
Trap chamber	6×10^{-8}	Turbo Pump (Varian, V250)

experiment. The turbo pump is backed up by an oil-free mechanical pump (Varian, TriScroll Dual Stage Dry Pump).

Between the chopper chamber and trap chamber is a 127-cm-long, 3.56-cm-diameter vacuum tube. Pressure in the trap chamber is 6×10^{-8} Torr in the experiment. The trap chamber is pumped by a turbo pump (Varian, V-250, pump speed 200 l/s for nitrogen). Pressures in chopper chamber and trap chamber are monitored by two ionization gauges, respectively. The Chopper chamber also houses a residual gas analyzer for monitoring the partial pressures of different gases in the vacuum system. The pressures and pumps in four vacuum chambers are listed in Table 4.2.

A novel feature of the vacuum system is that it can be switched into a mode, which repeatedly recirculates the krypton atoms through the vacuum system. This can be done with the turbo pump in the downstream chamber pumping the krypton gas back into the upstream chamber instead of the atmosphere, as shown in Figure 4.6. As a consequence, this recirculation mode can dramatically increase the system efficiency for trapping and counting the atoms.

4.4.2 Transverse Cooling

We use "two-dimensional transverse cooling" technique [58] to collimate the metastable krypton beam. In the transverse cooling chamber, the metastable krypton beam is cooled in both transverse directions by two sets of laser beams, each of which has a beam size of 1 cm $\times$ 2 cm and an intensity of 40 mW/cm^2. The laser beam is

multiply reflected between two flat mirrors (each size is 10 cm ×2 cm) and interacts with the metastable krypton atoms over 10 cm along the atomic beam flux once the atoms exit the discharge region. For each dimension, one of the two mirrors is mounted outside the chamber and is adjustable, the other is fixed inside the chamber.

With one-dimensional transverse cooling, we can enhance the trap loading rate by factor of 8. With two-dimensional transverse cooling, an enhancement factor of 20 to 25 can be achieved. Note that this process is isotopically selective; it only enhance the forward atomic beam flux and therefore the trap loading rate of the selected isotope. Also note that, when the laser frequency is tuned to the transition of odd isotopes of krypton, the sidebands in the transverse cooling light can optical pump the atoms in the states of $F = 11/2$ and $F = 9/2$ into $F = 13/2$ state for ^{83}Kr and ^{85}Kr (optical pump the atoms in the states of $F = 9/2$ and $F = 7/2$ into $F = 11/2$ state for ^{81}Kr).

4.4.3 Slowing Down the Atoms with Zeeman Slower

We use the "Zeeman Slowing" technique to longitudinally slow down the atomic beam. The required slowing magnetic field (see Equation 3.5) is produced by a tapered solenoid, which is wound with wires in many layers of different lengths (shown in Figure 4.7). Each layer is a uniform solenoid, which produces a magnetic field B_solenoid along the axis of the solenoid

$$B\_solenoid(z) = \frac{\mu_0 nI}{2}\left[\frac{Z_1 - z}{\sqrt{r^2 + (Z_1 - z)^2}} - \frac{Z_2 - z}{\sqrt{r^2 + (Z_2 - z)^2}}\right] \qquad (4.3)$$

where n is "turns per cm"; I is current; Z_1 is the position of one end of the solenoid; Z_2 is the position of the other end of the solenoid. The magnetic field produced by the tapered solenoid is the sum of the magnetic fields produced by each layer uniform solenoid. The parameters of the tapered solenoid, such as lengths of the layers and the current, need to be well designed in order to produce a smoothly varying magnetic field that can meet the requirement of slowing down the atoms.

Downstream from the chopper chamber, the metastable krypton atoms enter 50-inch-long Zeeman slower, where they are decelerated by a circular-polarized laser beam from

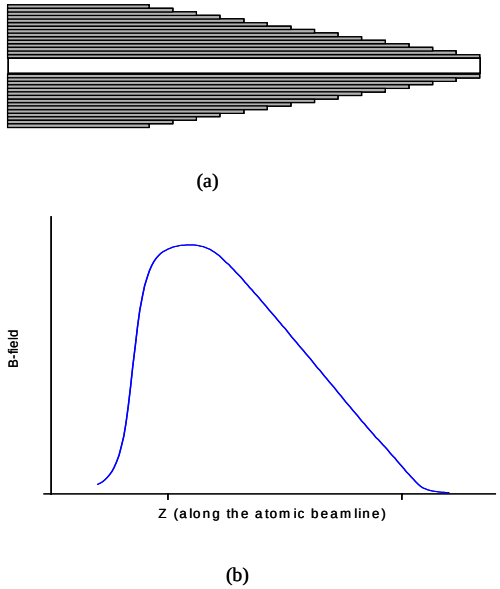

Figure 4.7 (a) Schematic of a Zeeman slower; (b) Slowing magnetic field profile.

a velocity of approximately 300 m/s near the source to 20 m/s as they enter the trap chamber. The laser beam (with a frequency of 360 MHz red-detuned to that of the trapping light) has an intensity of 5 mW/cm^2 in the trap chamber and is gently focused

from the trap chamber up to the discharge region. This schematic is applied to reduce the atomic beam divergence when the atoms are slowed down in the Zeeman slower.

4.4.4 Magneto-Optical Trap (MOT)

On the trap chamber, a pair of anti-Helmholtz coils (MOT coils) are wound to provide the quadrupole field required by the MOT, which has a field gradient of about 3 Gauss/cm along the horizontal axis (Figure 3.3). The equations on the magnetic field

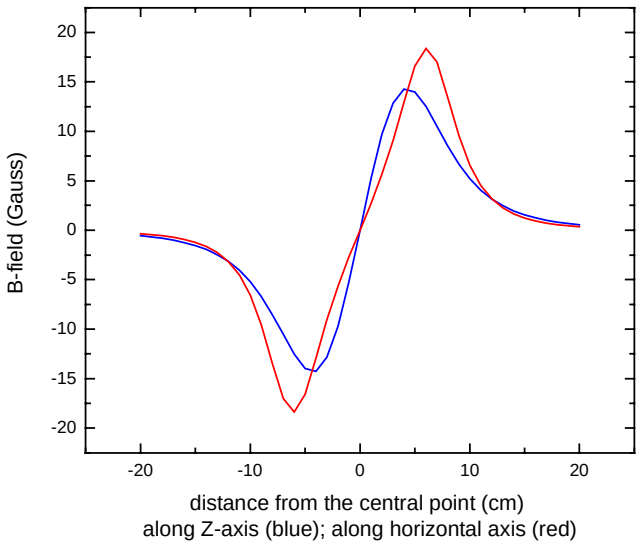

Figure 4.8 MOT field profile along the horizontal axis and vertical axis. In this calculation, coil radius $r = 6.35$ cm; distance between the two coils $d = 6.985$ cm; current $I = 50 \times 4$ Amp.

produced by the pair of coils are as follows. Along the z-axis (Figure 3.3), the magnetic field $B_z(z)$ is

$$B_z(z) = \frac{\mu_0}{4\pi}(2\pi r^2 I)\{[r^2 + (\frac{b}{2} - z)^2]^{-1.5} - [r^2 + (-\frac{b}{2} - z)^2]^{-1.5}\} \qquad (4.4)$$

where $\mu_0 = 4\pi \times 0.1$; r is radius of the coils; I is the current flowing through the coils; b is the distance between the two coils. Along the horizontal axis of MOT, the magnetic field $B_x(x)$ is

$$B_x(x) = \frac{\mu_0}{4\pi} r d \int_0^{2\pi} \frac{\sin(\theta)}{[r^2 + x^2 + \frac{d^2}{4} - 2xr\sin(\theta)]^{1.5}} d\theta \qquad (4.5)$$

Near the central point of the MOT, the gradient of magnetic field along the z-axis is about two times the gradient of magnetic field along the horizontal axis. A MOT magnetic field profile is shown in Figure 4.8.

The "End" coil, wound at the end of the atomic beamline, is used to compensate the residue magnetic field of the slowing solenoid at the center of the chamber. By tuning the current of the End coil, we can fine-tune position of the trap in the direction along the atomic beam. The "Horizontal-Trim" coils and "Vertical-Trim" coils are installed to fine-tune the position of the trap in the horizontal direction and in the vertical direction, perpendicular to the atomic beam.

Each of three pairs of trapping laser beams has an intensity of 10 mW/cm^2 and a beam size of 3 cm in diameter. The frequency of trapping light is 6 MHz red-detuned to the atomic transition.

4.4.5 Detection of Trapped Atoms

Since the trapping light is infrared, the trap can not bee seen by naked eyes. We use the Charged Coupled Device (CCD) camera to detect the fluorescence of the trapped atoms and the fluorescence image can be monitored on a monitor. With the CCD camera, we can qualitatively study the shape and the brightness of the trap.

To measure the number of the trapped atoms, we use a PIN Photo-diode (detection area is 20.4 mm^2, quantum efficiency is approximately 0.8 at 811nm) with a gain of 10^8 Ω. The detector is put in front of one viewport of the trap chamber and is 13 cm away from the trap. The geometric photon-collection efficiency is about 10^{-4}, i.e. every 1 out 10,000 photons emitted from the trapped atoms is collected by the PIN detector.

The number of trapped atoms reaches a maximum when the loading rate of atoms is equal to the loss rate of the atoms in the trap. Equation (4.2) describes the evolution of the number of trapped atoms during the loading period,

$$\frac{dN}{dt} = L - \frac{N}{\tau} - \beta N^2 \qquad (4.6)$$

where L is loading rate; the first loss term N/τ is due to the collisions between the trapped atoms and the thermal background atoms, τ is about 0.5 seconds when the pressure in the trap chamber is maintained at 6×10^{-8} Torr; the second loss term βN^2 is due to the collisions between pairs of trapped atoms. Generally speaking, when the loading rate is high ($\geq 10^8$ atoms/second), loss is dominated by the second loss term and the loading time (defined as the time taken to load 63% (1-1/e) of atoms under equilibrium into the trap) is short (~20 ms); when the loading rate is low, especially in the

condition of single atom detection (discussed in Chapter 5), the first loss term dominates and the lifetime of the single atom in the trap is about 0.5 seconds.

Therefore when we calculate a high trap loading rate using (4.2), we can drop the first loss term and only keep the second loss term. The solution is

$$N(t) = \sqrt{\frac{L}{\beta}} \frac{e^{2\sqrt{\beta L}t} - 1}{e^{2\sqrt{\beta L}t} + 1} \qquad (4.7)$$

The trap loading rate can be derived as follows. When the trap reaches the equilibrium,

$$N(t \to \infty) = \sqrt{\frac{L}{\beta}} \qquad (4.8)$$

This number of trapped atoms can be measured with the PIN detector. Then we measure the time difference Δt between when the trap reach 10% of the equilibrium trapped atom number and when the trap reach 50% of the equilibrium trapped atom number. Using (4.3), it is easy to get

$$2\sqrt{\beta L} = \frac{\ln \frac{27}{11}}{\Delta t} \qquad (4.9)$$

Combining (4.4) and (4.5), we have

$$L = 0.9 \frac{N(t \to \infty)}{\Delta t} \qquad (4.10)$$

Under the optimum condition, a ^{83}Kr trap loading rate of 3×10^9 atoms per second can be achieved with a trap loading time of 20 ms.

In the condition of single atom detection, the second loss term can be neglected in the calculation. Solving the equation (4.2), we have

$$N(t) = N_0(1 - e^{-t/\tau}) \qquad (4.11)$$

where $N_0 = L\tau$. The loading time is equal to τ.

5 Single Atom Detection

The isotopic abundances (I.A.) of ^{85}Kr and ^{81}Kr are approximately 2×10^{-11} and 6×10^{-13} [4, 9, 59], respectively. With the loading rate of ^{83}Kr (I.A.=11.5%) at 3×10^{9} atoms/s, we expect the loading rate for ^{85}Kr and ^{81}Kr to be between 10^{-3}/s and 10^{-1}/s. Since the lifetime of the trapped atoms is 0.5 seconds at a pressure of 6×10^{-8} Torr in the trap chamber, the rare krypton atoms do not accumulate in the trap; instead they are usually captured one at a time. Therefore, the system must be able to detect a single atom in the trap.

In single atom detection, the main technical challenge is to reduce the background photons scattered off walls, windows, and even the optics outside the vacuum chamber. It takes at least 10 mW of light to maintain the trap, while only 2 pW of light is emitted by a trapped krypton atom.

5.1 Spatial Filter

The schematic of the optical system for single atom detection is shown in Figure 5.1. Each of the four identical lenses has a diameter of 25 mm and a focal length of 50 mm. The lens closest to the trap is located inside the trap chamber and is 50 mm away from the trap. The other three lenses are installed along a tube. The single atom emits approximately 10^{7} photons per second, of which one percent are collected and imaged by one pair of the lenses, through an aperture (diameter is tunable, minimum is 0.6 mm)

which spatially filters out most of the diffuse background light, and re-imaged by another pair of lenses onto the detector. An electronic shutter (Melles Griot, 04 IES 211) is

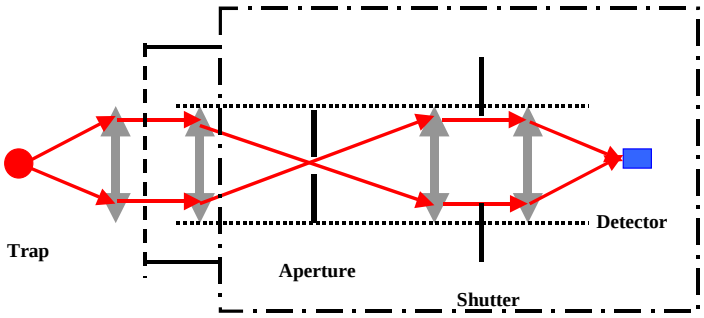

Figure 5.1 Schematic layout of the optical system for single atom detection. Dashed line is the viewport of the trap chamber; dotted line is the tube; dashed and dotted line is the electronics box.

installed in front of the detector and used to prevent the detector from over-exposure.

In order to reduce the scattering light from the chamber walls, the inner surface of the trap chamber is coated with a vacuum-compatible black paint. The paint material (AZ Technology, MLS-85SB) is specially designed for high vacuum systems (down to 10^{-11} Torr). In order to reduce the scattering light from the optics outside the trap chamber, all of the nearby mirrors and quarter-waveplates are carefully aligned, and sometimes deliberately mis-aligned.

5.2 Avalanche Photon Detector (APD) and Electronics

We use an APD (EG\&G SPCM-AQ-21) as the single atom detector. The APD has a dark count of 860 counts/s and a pulse_width of 30 ns. The quantum efficiency at 811nm is 25% and the detection active area is 0.5 mm in diameter. The APD has a gating function: when the voltage in the gate input is TTL-high (5 V), the detector is enabled; when the voltage is TTL-low, the detector is disabled. Based on this function, a protection circuit is used to prevent the APD from damage due to over-exposure. The maximum count rate of the APD is 13 MHz.

The APD is housed in an electronic box, whose inner walls are also covered with the black paint to reduce the scattering background. Inside the box, the APD is installed on a three-axis translation stage (Newport, 423 series) which can be used to fine-adjust the position of the APD. The resolution of the translation stage in each axis is 1 μm.

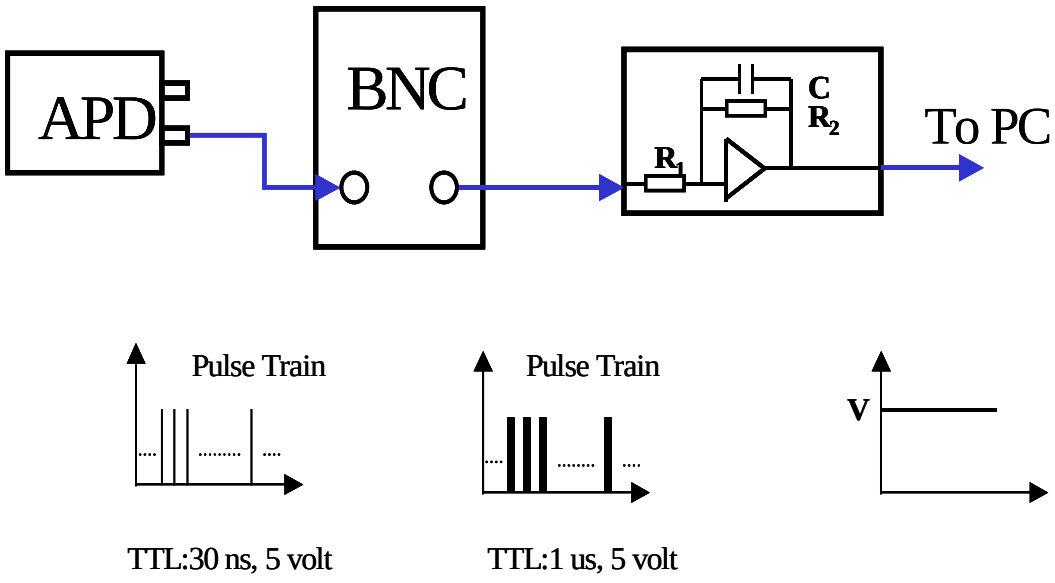

Figure 5.2 Electronics for single atom detection.

Figure 5.2 shows the electronics for single atom detection, which can convert photon count rate into a voltage output. The APD detects a train of photons and converts it into a train of electronic TTL pulses (30 ns, 5 Volt). A pulse generator (Berkeley Nucleon Corporation, Model 8010) expands the TTL pulses from 30 ns to 1 μs (pulse_width is adjustable). An integrator circuit then integrates the train of the pulses in time and converts the pulse signals into a voltage signal V at its output,

$$V = -\frac{R_2}{R_1} \cdot (1\mu s) \cdot P \cdot (5Volt) \qquad (5.1)$$

where R_1 and R_2 are the input and feedback resistors in the integral circuit; 1 μs and 5 Volt are the pulse_width and the amplitude of the TTL signal at the input of the integral circuit; and P is the photon counting rate. In our integrator circuit, R_1=15 kΩ, R_2=33 kΩ, the capacitor C=0.33 μF; the integration time is 10 ms. For a 20 kHz photon counting rate, the voltage signal is about 200 mV.

5.3 Single Atom Signal

Before we could count individual ^{85}Kr and ^{81}Kr atoms, we optimize the conditions of single atom detection by obtaining clear ^{83}Kr single atom signals.

The optimal conditions for single atom detection are quite different from the optimal trap loading conditions. To achieve a high loading rate, we use large (3 cm in diameter) and strong (10 mW/cm^2) trapping laser beams and a moderate magnetic field gradient of the MOT (8 Gauss/cm). However, when detecting, in order to reduce the scattering light,

both the diameter and intensity of each laser beam are reduced to 1 cm and 2 mW/cm^2, respectively. Meanwhile, in order to squeeze the trapped atom into a smaller volume (about 0.5 mm across) and increase its image brightness, the field gradient is increased to 16 Gauss/cm.

Since the typical trap loading rate for ^{83}Kr is ~10^9 s^{-1}, we need to decrease the loading rate to a few atoms per second or even lower to see a single atom in the trap. This can be done by reducing the rf power of the discharge, blocking the transverse cooling light, and changing the polarization of the slowing light to reduce its effectiveness in slowing down the metastable krypton atoms.

Each atom in the trap emits approximately 10^7 photons per second. With the

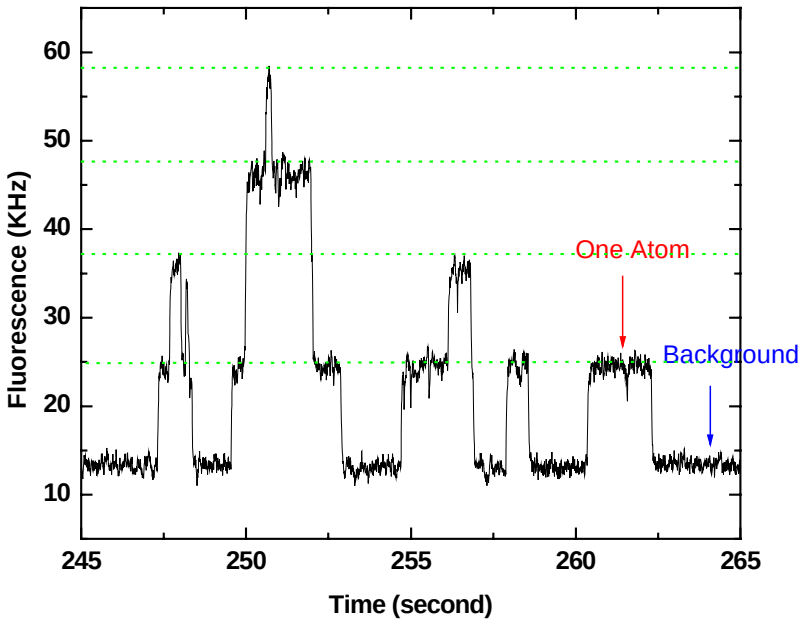

Figure 5.3 ^{83}Kr single atom signals.

combination of geometric efficiency (1%) and the quantum efficiency of the APD (25%), the ideal single atom signal is about 25 kHz. Figure 5.3 shows the ^{83}Kr single atom signals we recorded. The single atom signal is 13 kHz and the background is 13 kHz. The signal to noise ratio of 15 with 10 ms integration time is achieved. In the figure, one, two, three, and four atoms in the trap can be clearly identified.

6 Counting Individual ^{85}Kr and ^{81}Kr Atoms

Since the isotopic abundance of rare krypton atoms is very low, we need to run the system at the maximum trap loading rate. Meanwhile, we also need to detect single atoms in the trap. However, as we discussed in the last chapter, the trap loading conditions are significantly different from the single atom detection conditions. In order to meet these two sets of requirements, switching between "capture mode" (trap loading) and "detection mode" (single atom detection) is needed when we detect ^{85}Kr and ^{81}Kr in the trap.

6.1 Switching Between Capture Mode and Detection Mode

The optimal conditions for trap loading and single atom detection are listed in Table 6.1,

Table 6.1 The optimal conditions for trap loading and single atom detection.

	Capture Mode	Detection Mode
Diameter of trapping beams	3 cm	1 cm
Intensity of trapping beams	10 mW/cm^2	2 mW/cm^2
MOT field gradient	8 Gauss/cm	16 Gauss/cm
Atomic beam	On	Off
APD detector	Off	On

A schematic diagram of trapping light switching is shown in Figure 6.1. The switching

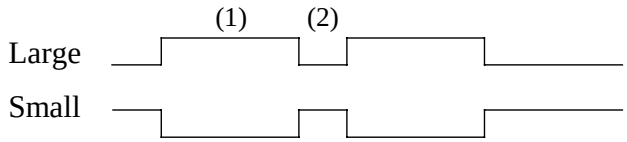

(1) Large beam is ON; small beam is OFF

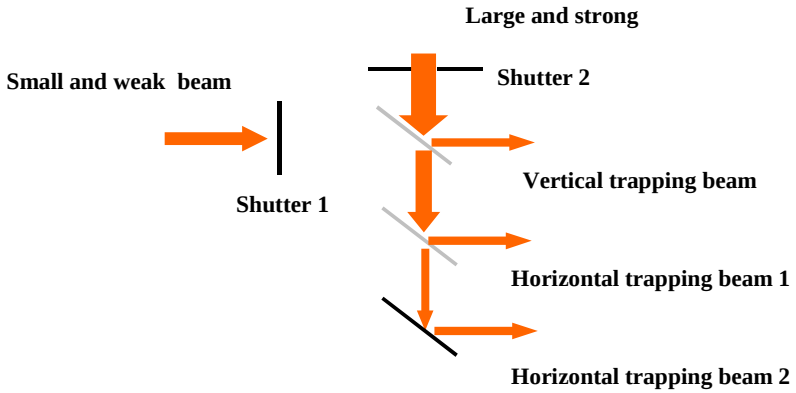

(2) Large beam is OFF; small beam is ON

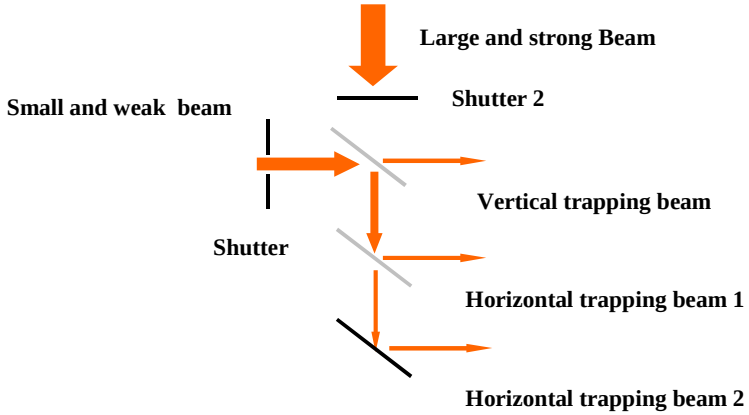

Figure 6.1 Schematic of trapping light switching.

is accomplished with two electronic shutters (Vincent Associates, LS3T2), each of which has a rise time of less than 1 ms and is controlled by a Uniblitz 212 shutter controller. The controller is triggered by an external TTL input, which determines the shutter exposure and closure time. In the figure, Beamsplitter 1 distributes 40% of the large beam into the vertical trapping light, the other 60% goes to the horizontal trapping light. Beamsplitter 2 is 50/50. In the capture mode, the large beam (vertical - 16 mW/ cm^2, each horizontal - 12 mW/ cm^2) is on while the small beam is off; in the detection mode, the small beam (vertical - 6 mW/ cm^2, each horizontal - 2 mW/ cm^2) is on while the large beam is off.

Switching of magnetic field gradients is accomplished with a high-current switching

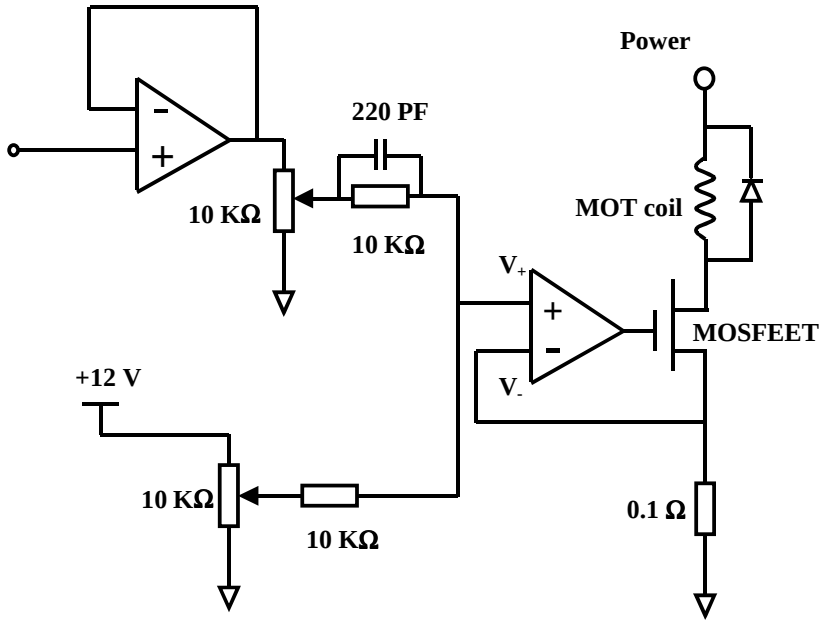

Figure 6.2 Schematic of high-current switching system. $I = \frac{V_{-1}}{0.1}$, $V_- = V_+$.

system. The schematic is shown in Figure 6.2. The MOT coil current I is controlled by an external TTL input with a MOSFET (BUK 453-60A).

When the input is TTL-high (5 Volt), V_- is high and as a result the current is large (13 A in the experiment); when the input is TTL-low (zero), V_- is low and the current is small (5 A in the experiment). In this system, a diode is used to relieve the current when switching is from large current to small current. Since the large current runs through the MOSFET and 0.1 Ω resistor, the electronics board becomes hot in a long run and therefore a heat sink or a fan is needed. The 0.1 Ω resistor (OHMITE 850-RE75G series) has a high stability (±90 ppm/degree), which is important in order to keep the two current conditions highly stable. In our one-day experimental run, the large current and small current are both stable within 0.005 Ampere. The response time of the current switching is 4 ms.

An electronic shutter is installed in front of the APD detector to protect the detector from overexposure. In the capture mode, the shutter is closed; in the detection mode, the shutter is open.

When switching from capture mode to detection mode, the atomic beam is turned off in order to eliminate the scattering light off the atomic beam in the trap chamber. This is realized with an "Atomic Chopper", whose schematic is shown in Figure 6.3. This mechanical chopper consists of an in-vacuum stepper motor (MDC, SM23-HV, vacuum range 5×10^{-8} Torr) and a U-shape blade symmetrically mounted on the top of the stepper motor axis. When the stepper motor is in operation, the blade will be rotating

along the axis. The atomic chopper is installed inside the chopper chamber and can periodically block the metastable krypton beam, essentially turning on and off the beam going into the trap chamber.

Figure 6.3 also shows that the slowing light will be chopped while the atomic beam is being chopped. A photodetector is installed in front of the viewport on the source chamber to receive the chopped slowing light signal, which is then shaped into a TTL signal. The TTL signal, as a trigger input, is sent to a pulse generator (BNC, Model 500A), which has four output channels to control switching of the laser beams, MOT coil current switching, and switching (on and off) of electronic shutter in front of the APD. With this schematic, all the switching is synchronized to the position of the atomic chopper.

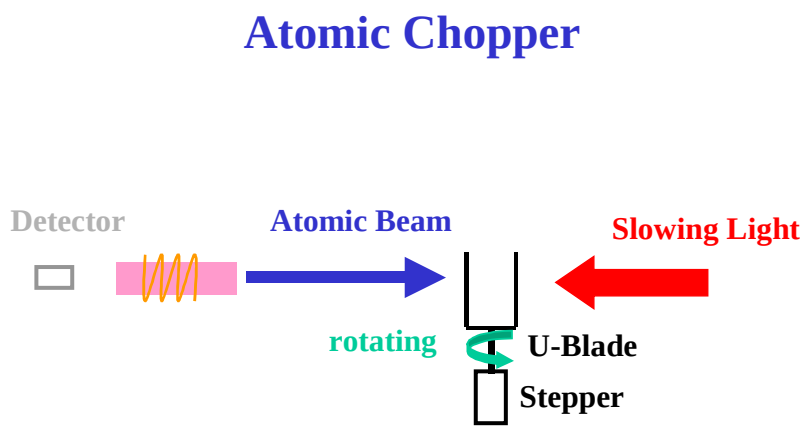

Figure 6.3 Schematic of "atomic chopper", which is a mechanic chopper consisting of a stepper motor and a U-shape blade mounted on the tip of the stepper motor.

The timing diagram of TTL signal at the input and the four synchronized outputs is shown in Figure 6.4. The rotating period of atomic chopper is determined by the stepper motor speed, which is adjustable. In our experiment, the period is 385 ms. The duty cycle of the trigger input is determined by the shape of the U-shape blade. In the experiment, the atomic beam ``ON" time is 285 ms, "OFF" time is 100 ms.

For each channel output of BNC, the pulse_width and delay to the trigger input can be

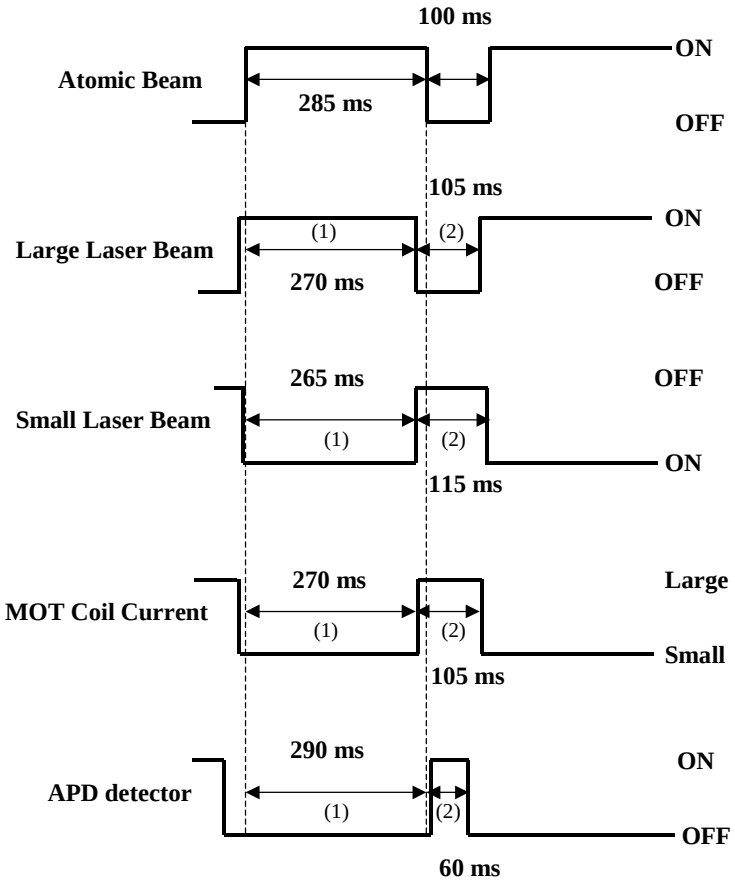

Figure 6.4 Timing diagram of BNC input and outputs. The "useful" period is (1)+(2).

set independently. Note that the "useful" period (from the rising edge of the trigger input to the time when the channel output is back to its initial state) of each channel is set to be a few milliseconds shorter than the period of the trigger input. If the "useful" period is longer than the trigger period, the channel will not be triggered by the rising or falling edge of the next TTL pulse until it finishes its current period, which will result in the channel idling for the next period.

Another note is that the large trapping laser beam and small trapping laser beam cannot be off at the same time during switching, or the trapped atoms will escape due to the interruption of trapping laser beams. In order to avoid that, we set up 5 ms overlapping time between large beam and small beam.

Moreover, in order to keep the strong scattering background due to the large laser

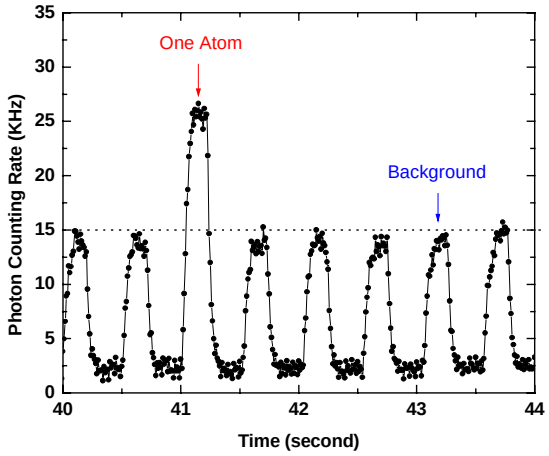

Figure 6.5 ^{85}Kr single atom signal. Time constant of the circuit is about 10 ms and the signal to noise ratio is 15 within 10-ms integration time.

beams or the atomic beam fluorescence from falling into the detector exposure time period, 60 ms "ON" time for APD is set much shorter than any other detection time parameters.

6.2 ^{85}Kr and ^{81}Kr Single Atom Signal

^{85}Kr single atom signals are shown in Figure 6.5. The signals are the output of the integral circuit (in Chapter 5) and the time constant of the circuit is about 10 ms. The single atom signal is about 13 KHz and the background is 15 KHz. In the loading period, the APD detector is blocked and about 2 KHz background is mainly due to the dark current.

6.3 Computerized Data Acquisition

Single atom signals at the output of integral circuit can be monitored and recorded by both oscilloscope and computer. But since signals at the output of the integral circuit are analog, the size of data acquired and recorded by computer is very large and therefore requires a significant fraction of CPU time to process and a large amount of memory to store.

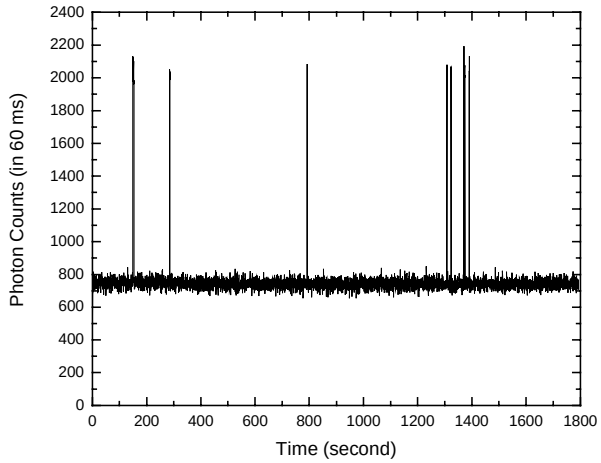

(a)

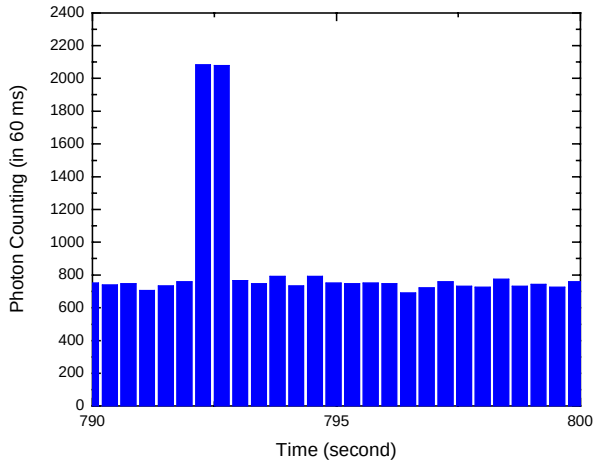

(b)

Figure 6.6 ^{81}Kr single atom signal with new schematic of data acquisition. Upper graph is a 30-minute time train of atom counting of ^{81}Kr; lower graph is a zoom-in picture in 10 seconds. Signal to noise ratio is greater than 45.

To solve the problem, a new schematic of data acquisition was implemented including

a PC and National Instruments' LabView instrumentation. A LabView interface board is configured to read two digital inputs. One input (Gate) is gate signal that is the same as the signal sent to the electronic shutter in front of APD (details in chapter 5). The other input (Atom Count) is the TTL signal directly from the output of the pulse generator (Chapter 5). For each period of atom counting, the PC counts the number of TTL pulses when "Gate" is TTL-high; it stops counting when "Gate" is TTL-low. Single atom counting of ^{81}Kr is shown in Figure 6.6. The signal is the TTL pulse number (also the photon number) counted by PC in 60 ms. The upper graph is 30-minute time train of atom counting of ^{81}Kr. The lower graph is a Zoom-in picture in 10 seconds. With this schematic, the signal to noise in integration time of 60 ms is greater than 45.

7 ^{85}Kr and ^{81}Kr Abundance Measurement

In ^{81}Kr-dating, age is defined as the time since water or ice sample was near the surface and had contact with the atmosphere. Once the water went underground and ice froze, they were separated from the atmosphere, and the ^{81}Kr abundance started to decrease according to

$$N(t) = N_0 e^{-t/\tau} \qquad (7.1)$$

where τ is the lifetime of ^{81}Kr, N_0 is the atmospheric isotopic abundance of ^{81}Kr, N(t) is the isotopic abundance of ^{81}Kr in the sample, and *t* is the age of the sample.

7.1 Control Isotope and Ratio Measurements

The isotopic abundance of ^{81}Kr can be determined by the ratio of the trap loading rates of ^{81}Kr and a control isotope with known isotopic abundance. The trap loading rate of an individual isotope depends on the isotopic abundance and many parameters of the apparatus including the discharge intensity, gas flow rate, various vacuum pressures, partial pressure of krypton, laser beam intensity, laser frequencies, laser beam alignment, etc. Our system is stable after about half an hour of warm-up. The loading rate for ^{83}Kr typically drifts less than 15% in a 10-hour run. By frequently switching the system between counting ^{81}Kr and counting the control isotope, much of the common mode noise due to the variation of all the parameters is cancelled out in the ratio. Furthermore, the age is determined by the ratio of the isotopic abundance of ^{81}Kr in the sample and in

the atmosphere; in fact it is a measurement of a ratio of ratios, which further reduces the systematic effects.

In principle, the stable ^{83}Kr can be used as the control isotope. But in practice, its trap loading rate ~10^9 atoms/s is so much higher than that of ^{81}Kr that, instead of single atom detection, it requires a different detector system such as a low gain pin photo-diode detector to measure the fluorescence of the trapped ^{83}Kr atoms. Meanwhile, due to the collisions between pairs of trapped atoms, the trap lifetime of ^{83}Kr (20 ms) is much shorter than that of a single trapped ^{81}Kr atom (~0.5 second). These differences make ^{83}Kr a less reliable control isotope. On the other hand, ^{85}Kr with the isotopic abundance of ~10^{-11}, can be introduced into the sample and calibrated accurately with the LLC method. The "spiked" ^{85}Kr can then be counted at the single atom level and serve as a reliable control isotope. The age of the sample can be calculated as

$$t = \tau \ln\left[\frac{N_{81a}/\left(N_{85a}/\rho_{85a}\right)}{N_{81s}/\left(N_{85s}/\rho_{85s}\right)}\right] \qquad (7.2)$$

where N_{81s} and N_{81a} are counting rates of ^{81}Kr atoms from the sample and from air, respectively; N_{85s} and N_{85a} are counting rates of ^{85}Kr atoms from the sample and air, respectively; ρ_{85s} and ρ_{85a} are LLC calibration of ^{85}Kr isotopic abundance from the sample and air, respectively. The spike and LLC of ^{85}Kr involve mature technologies that are practiced on a routine basis in a few selected labs around the world.

7.2 Laser Frequency Mapping

Laser frequency setting affects the trap loading rates; it affects the abundance

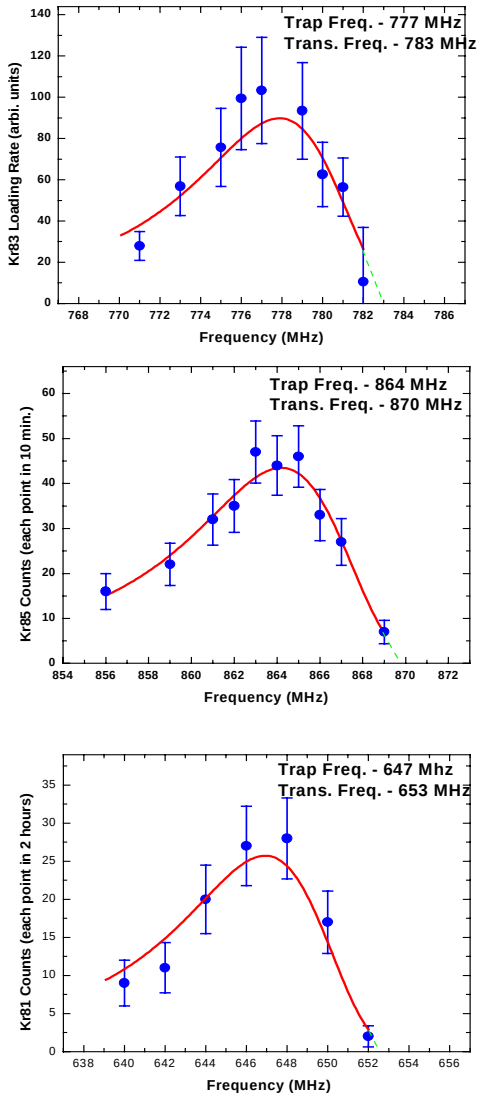

Figure 7.1 Frequency Mapping. **(a)** ^{83}Kr loading rate vs. trapping frequency; **(b)** ^{85}Kr loading rate vs. trapping frequency, a 10-minute measurement is taken for each data point; **(c)** ^{81}Kr loading rate vs. trapping frequency, a 2-hour measurement is taken for each data point.

measurement, which is done by measuring ratio of trap loading rates of two different isotopes; but it should not affect the age, which is derived from the isotopic abundances of two samples ideally analyzed under identical laser frequency settings. Therefore, the repeatability of laser frequency setting from one run to another is crucial to age determination. A drift in laser frequencies can lead to a systematic error in age. The significance of this effect can be studied by mapping out the laser frequency dependence of trap loading rate of ^{83}Kr, ^{85}Kr and ^{81}Kr. Furthermore, in order to count the atoms at the maximum trap loading rate, we need to find out the optimum laser frequency settings.

From Figure 7.1(a), we conclude that the optimum trapping frequency for ^{83}Kr is 6 MHz red-shifted from its transition frequency. For ^{85}Kr (Figure 7.1(b)), the maximum loading rate is about 45 atoms in 10 minutes. The optimum trapping frequency is about 864 MHz blue-shifted to the ^{84}Kr transition $5s[3/2]_2 \rightarrow 5p[5/2]_3$. If we assume that the optimum trapping frequency for ^{85}Kr is also 6 MHz red-tuned to its transition, we can derive that its transition frequency is 870 MHz blue-shifted to the ^{84}Kr transition. For ^{81}Kr (Figure 7.1(c)), the maximum loading rate is about 14 atoms in an hour. The optimum trapping frequency is 647 MHz blue-shifted to the ^{84}Kr transition. Its transition frequency is 653 MHz blue-shifted to the ^{84}Kr transition if we use the same assumption as for ^{85}Kr. Our transition frequency results are in good agreement with that measured by Cannon [51]. The laser frequency, locked to the $5s[3/2]_2 \rightarrow 5p[5/2]_3$ transition of ^{84}Kr in the vapor cell, has a repeatability of better than 0.5 MHz, which should cause the trap loading rate to shift by less than 4%.

We have also mapped out loading rate vs. 1st sideband and loading rate vs. 2nd sideband for both ^{83}Kr and ^{85}Kr. The results (listed in Table 7.1) are also in good agreement with Cannon's work. For either isotope, the loading rate drops by factor of 2 when either 1st sideband frequency is tuned 20 MHz away from its optimum frequency or the 2nd sideband is 40 MHz away from the optimum frequency. This broad frequency dependence is due to power broadening; the rates of repumping transition provided by the

Table 7.1 Frequency Comparison between Cannon's work and this work.

	Cannon's work	This work
^{83}Kr - transition	786.9 MHz	783 MHz
^{83}Kr - 1st sideband	-88.9 MHz	-87 MHz
^{83}Kr - 2nd sideband	-711.8 MHz	-707 MHz
^{85}Kr - transition	868.7 MHz	870 MHz
^{85}Kr - 1st sideband	-76.4 MHz	-78 MHz
^{85}Kr - 2nd sideband	-687.2 MHz	-676 MHz
^{81}Kr - transition	651.8 MHz	653 MHz
^{81}Kr - 1st sideband	-308.5 MHz	
^{81}Kr - 2nd sideband	-795.9 MHz	

laser intensity of the sidebands far exceed the needed repumping transition rates. We

conclude that the effect on trap loading rates due to any changes of sidebands is negligible.

7.3 Switching Between Different Isotopes

From measuring one isotope to the other, there are only three parameters to switch: isotope shift which is controlled by the AOM frequency and the two sideband frequencies which are controlled by the EOM frequencies. These switches are performed either manually or automatically with computer control.

8 An Atom Trap System For Practical ^{81}Kr-dating

As we discussed in chapter 2, due to its extremely low isotopic abundance, there are only roughly 1,000 ^{81}Kr atoms in one liter of groundwater. Moreover, due to the low concentration of krypton in the atmosphere, only approximately 60 μl STP of krypton can be extracted from 1,000 liters of groundwater. For practical ^{81}Kr-dating of groundwater, 20,000 liters of groundwater may be the upper limit for practical Earth Sciences studies. That amount of groundwater provides approximately 400 μl STP of krypton gas sample, in which there are only 2×10^{7} ^{81}Kr atoms. A 10% measurement of that krypton gas sample requires the analysis system to achieve system efficiency larger than 1×10^{-5}. Meanwhile, the system also needs to operate with krypton samples as small as a few hundred μl STP.

8.1 Gas Handling System

Figure 8.1 shows the schematic of gas handling system, which is designed to operate with small gas samples (~100 μl STP).

The sample is contained in a metal cell with a NuPro valve, which can be attached to one end of the reservoir, as shown in Figure 8.1. The reservoir has a volume of 475 ml and when 100 μl STP of krypton gas sample is released into the reservoir, the pressure in the reservoir rises to about 150 mTorr. The maximum amount of sample gas that can be measured with the Baratron gauge in the reservoir is approximately 500 μl STP. The gas

sample is injected from the reservoir into the source chamber through a fine leak valve (Granville-Phillips, 216 Servo Driven Valve Assembly), which is operated by a flow controller (Granville-Phillips, Model 216). A fill of 30 µl STP of krypton gas into the

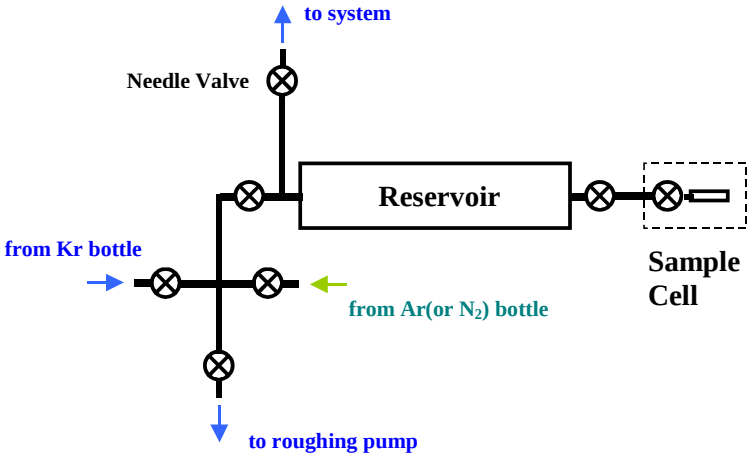

Figure 8.1 Schematic of a gas handling system developed to handle small krypton gas samples (~100 µl STP).

vacuum system will increase the source chamber pressure to 4 mTorr, which is optimal for rf discharge operation.

The reservoir is also connected to a bottle of commercial krypton gas, which is routinely used to check and to optimize the system. The argon (or nitrogen) gas bottle connected to the reservoir is used to flush the system (discussed later). The reservoir can be pumped by a roughing pump through a long pipe or by a turbo pump through the vacuum system.

8.2 Gas Recirculation

When the vacuum system is operated in recirculation mode, the krypton gas sample is repeatedly recirculated through the vacuum system and therefore the system counting efficiency can be dramatically improved. A schematic of gas recirculation is shown in Figure 8.2.

In each stage of gas recirculation, a turbo pump pumps the krypton gas through a vacuum tube from the downstream chamber back to the upstream chamber (stage 1: from transverse cooling chamber to source chamber; stage 2: from chopper chamber to transverse cooling chamber; stage 3: from trap chamber to transverse cooling chamber).

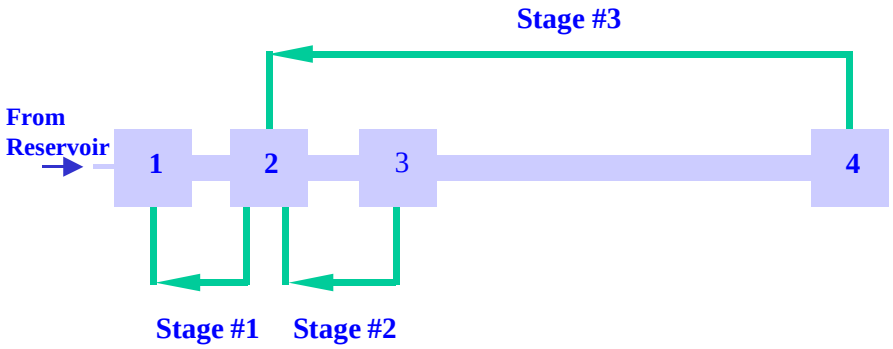

Stage #1: source chamber - 4 mTorr; transverse cooling chamber - 2×10^{-5} Torr;
Turbo pump - 270 l/s; tube conductance 12 l/s.
recirculation tube - 12 inch long, 3/2 inch in diameter.
Stage #2: chopper chamber - 4×10^{-7} Torr;
Turbo Pump - 150 l/s; tube conductance 0.9 l/s.
recirculation tube - 24 inch long, 3/4 inch in diameter.
Stage #3: trap chamber - 6×10^{-8} Torr;
Turbo Pump - 200 l/s; tube conductance 0.3 l/s.
recirculation tube - 84 inch long, 3/4 inch in diameter.

Figure 8.2 Schematic of gas recirculation.

The vacuum tubes need to be properly chosen in order to minimize the amount of krypton gas stored in the recirculation loops. There are two factors to be considered: one is the volume of the recirculation loop, the other is the pressure in the loop. On one hand, using thin tubes will reduce the volume of the loop, thereby decrease the amount of krypton gas accumulated in the loop. But on the other hand, thin tubes have small conductance, which will make a large amount of gas accumulate in the back of turbo pump, where the pressure is much higher than the chambers. The conductance of the vacuum tube should be compatible with the pumping speed of the turbo pump and can be calculated by

$$C = \frac{\frac{1}{4}\upsilon A}{1+\frac{3}{8}\frac{L}{R}} \qquad (8.1)$$

where C is conductance; υ is velocity of the thermal atoms (300 m/s for krypton atoms at room temperature); A is the cross sectional area of the tube; L is length of the tube; R is radius of the tube.

In our system, the tube conductance C_1 in the first stage is about 12 l/s; in the second stage, C_2 is about 0.9 l/s; in the third stage, C_3 is 0.3 l/s. To operate the whole vacuum system with the optimal pressures, we need to fill 30 μl STP of krypton gas into the system. And we estimate that there is approximately 10% of krypton gas in the recirculation loops.

Without the gas recirculation, the total counting efficiency is about 1×10^{-7}. With the first stage of recirculation, the system efficiency is increased to about 8×10^{-6}; with the first two stages of recirculation, the efficiency is about 4×10^{-5}; and with all three stages of recirculation, we achieve an system efficiency of 2×10^{-4} in 7 hours for 30 μl STP of krypton sample.

Ideally the krypton sample can be recirculated indefinitely in the system, however the run time is limited for two reasons: cross-sample contamination (discussed later) and argon outgassing.

When the system is in recirculation mode, the getter pump is the only pump for the system. As we discussed in chapter 4, it can pump nitrogen at the speed of 100 l/s. It can also efficiently remove other reactive gases, such as water and CO_2, while leaving the noble gases including krypton intact. Argon is an abundant noble gas and will accumulate due to outgassing in the vacuum system. We use a RGA (Residual Gas Analyzer) to monitor the pressures of different gases in the vacuum system. Over 10 hours, the partial pressure of argon in the chopper chamber can increase from below 10^{-9} Torr up to 1×10^{-7} Torr, or 50% of the krypton pressure. As a result, the krypton metastable beam flux is reduced and so is the trap loading rate. This effect requires the system to be pumped out after 10 hours of recirculation. The loss of krypton sample during the pumping-out limits the average times of recirculation to ~3000, and the counting efficiency of the system to 3×10^{-4}.

8.3 Cross-sample Contamination

When the rf-discharge is on, a small fraction of krypton atoms are ionized, accelerated by the rf field, and imbedded into the surface of the glass tube. Meanwhile, the previously embedded krypton atoms are released into the vacuum by the discharge. We observe an initial reduction of 3 μl STP of krypton, or 10% of the sample in one fill, within the first two hours after the discharge is turned on, and a total reduction of 6 μl STP, or 20% of one fill, in 8 hours. The loss rate gradually decreases to zero as the krypton atoms in the vacuum reach equilibrium with the embedded krypton atoms. We maintain a constant krypton pressure by refilling a few percent of krypton gas periodically throughout the experiment.

Obviously the embedded krypton atoms would be a serious source of cross-

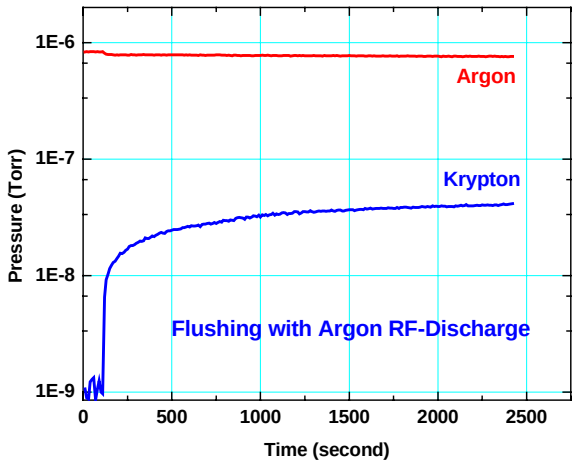

Figure 8.3 Cross-sample contamination

contamination. This is confirmed in the following test. After one measurement, the system is pumped out and filled with argon. The krypton pressure dramatically increases when the argon discharge is turned on, as shown in Figure 8.3. The amount of krypton released is measured to be 3 μl STP in half an hour.

We solve the contamination problem by flushing the glass tube with the discharge of

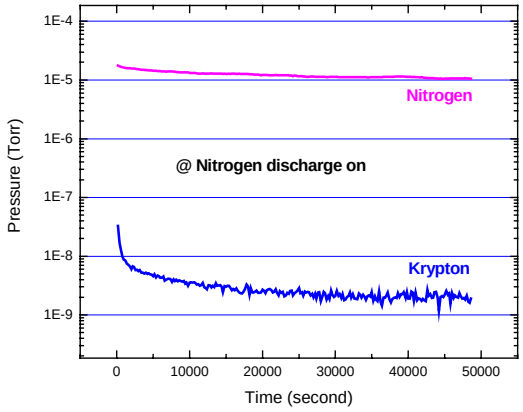

(a)

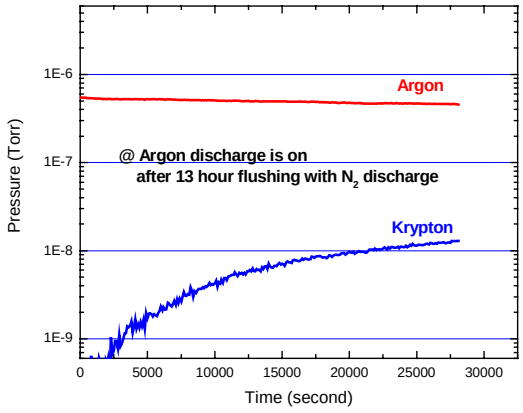

(b)

Figure 8.4 Flushing with the discharge of nitrogen. (a) flushing for 13 hours; (b) after flushing, the krypton pressure increase up to 1.3×10^{-8} Torr, which is about 7% contamination.

nitrogen or argon. We use nitrogen as the "cleaner" because nitrogen can be removed by the getter pump. The result is shown in Figure 8.4. We first flush the glass tube with nitrogen discharge for more than 13 hours. Then we turn on the argon discharge to see the krypton contamination after the flushing. In eight hours, the krypton pressure increases up to 1.3×10^{-8} Torr, which is about 7% contamination. Note that the average contamination in a run is 50% of the final contamination level.

The effect of contamination on the $^{81}Kr/^{85}Kr$ ratio measurement can be expressed as follows,

$$r = r' + (r' - r^0)\varepsilon \qquad (8.2)$$

where r is the actual ratio of the krypton sample; r' is the measured ratio of the krypton sample; r^0 is ratio of the krypton contaminant (depending on the history of measurements); ε is the contamination level. Furthermore the ratio of modern krypton $^{81}Kr/^{85}Kr$ ratio to sample $^{81}Kr/^{85}Kr$ ratio can be derived as

$$\frac{r^0}{r} = \frac{r^0}{r' + (r' - r^0)\varepsilon} = \frac{r^0}{r'}\frac{1}{1-(\frac{r^0}{r'}-1)\varepsilon} \qquad (8.3)$$

The effect of contamination on age determination can then be expressed as follows,

$$t = \tau \ln\left[R' \frac{1}{1-(R'-1)\varepsilon}\right] \qquad (8.4)$$

where t is the age of the sample; τ is the lifetime of ^{81}Kr; $R' = \frac{r^0}{r'}$; ε is the contamination percentage.

9 ATTA vs. LLC -- Double-Blind Test

Our system has achieved a system efficiency of 2×10^{-4} and is capable of operating with the krypton gas sample as small as 30 μl STP. In order to demonstrate the capability of our system on quantitative measurements, we measured the $^{85}Kr/^{81}Kr$ ratios of a group of krypton gas samples prepared by Purschert *et al.* at the University of Bern, Switzerland. All of these samples are derived from young air samples (less than 80 years old) and therefore the isotopic abundances of ^{81}Kr are expected to be identical. On the other hand, the abundances of ^{85}Kr were prepared to be different and were measured with LLC at University of Bern. Note that, for each sample, we did not know the ^{85}Kr abundance measured with LLC until we finished our ratio measurement and sent our result to Bern for comparison. Therefore, the test is indeed "double-blinded".

9.1 Procedures

Each time before we start to analyze a new sample, we flush the system with nitrogen discharge for at least 10 hours in order to reduce the cross contamination below approximately 3%.

In an analysis, the system is filled with approximately 30 μl STP of krypton sample and run for typically 6 hours. An analysis run consists of many (averagely 8) cycles, with each cycle taking 40 minutes: 30 minutes for counting ^{81}Kr followed by 10 minutes for counting ^{85}Kr.

After 6 hours, argon will accumulate due to its outgasssing so that the partial pressure in the chopper chamber increases up to approximately 6×10^{-8}, or 30% of the krypton pressure. We then pump out and refill the system for another analysis run.

For each sample, we perform several analysis runs that mainly depend on the sample size and precision requirement.

9.2 Results and Data Analysis

We measured the first three test samples (O1, O2, O3) from 09/28/02 - 10/02/02. We analyzed one sample (ANL) from a bottle of commercial krypton gas and four more test samples (F1, F2, F3, F4) in February 2003. We analyzed the last test sample (M1) from University of Bern in March 2003. The results are shown in Table 9.1.

Column 2 lists the sample size of each krypton gas sample. Column 3 lists the sample volume we actually used. Generally speaking, 100 μl STP of krypton gas is a favorable size for our system, but we can also operate with as small as 30 μl STP of krypton sample. Column 4 lists the total number of analysis cycles for each sample. Column 5 is the number of ^{81}Kr atoms being counted for each sample. Column 6 is the number of ^{85}Kr atoms being counted for each sample. Column 7 is the ^{85}Kr/^{81}Kr ratio of each sample. The error is determined using the formula

$$\left(\frac{\delta R}{R}\right)^2 = \left(\frac{\delta C_{85}}{C_{85}}\right)^2 + \left(\frac{\delta C_{81}}{C_{81}}\right)^2 \qquad (9.1)$$

where R is the $^{85}Kr/^{81}Kr$ ratio and $R = 3C_{85} / C_{81}$, δR is the error of the ratio; C_{85} is the

Table 9.1 Rusults of test sample measurements.

Sample	Volume (μl STP)	Used Volume (μl STP)	# of runs	# of ^{81}Kr	# of ^{85}Kr	Ratio of $^{85}Kr/^{81}Kr$	LLC (dpm)
O1	167	113	28	166	231	4.17±0.42	14.4±1.6
O2	63(1)	40	16	94	525	16.8±1.9	85±5
O3	122	65	26	165	213	3.87±0.40	14.4±1.6
ANL	(2)	(3)	24	121	659	16.3±1.6	59±3.2
F1	86	75	15	61	405	19.9±2.7	64.9±5
F3	198	56	22	113	255	6.77±0.77	27.7±1.1
F2 (PreBomb)(4)	>600	(5)	17	79	17	0.65±0.17	(6)
F4	118	71	30	127	802	18.9±1.8	74.2±4
M1	442	61	20	84	365	13.0±1.6	45±3
M2 (spiked PreBomb)(7)	296	171	48	158	1254	23.8±2.0	81.2±5

This sample is not pure krypton gas, but a mixture of 40 μl STP of krypton and 23 μl STP of air.

(1) Sample "ANL" is from a bottle of commercial krypton gas.

(2) We did not measure the sample volume we consumed.

(3) The PreBomb sample was extracted from the the atmosphere by a German company before 1945 (between 1933 and 1940).

(4) Since the sample size is larger than 500 μl STP, the Baratron gauge cannot read the pressure in the reservoir and therefore we could not measure the sample volume we consumed.

(5) LLC of this sample shows the decay rate of 85Kr is less than 0.8 dpm.

(6) This sample is also made from the same reservoir as "F2"..

number of ^{85}Kr counts, δC_{85} is the statistical error of C_{85} ($\delta C_{85} = \sqrt{C_{85}}$); C_{81} is the number of ^{85}Kr counts, δC_{81} is the statistical error of C_{81} ($\delta C_{81} = \sqrt{C_{81}}$). Column 8 is the results of ^{85}Kr abundance measured with LLC at University of Bern.

^{85}Kr/^{81}Kr ratios measured with ATTA vs. ^{85}Kr/Kr ratios measured with LLC is plotted out in Figure 9.1. A fitting line is also shown in the figure.

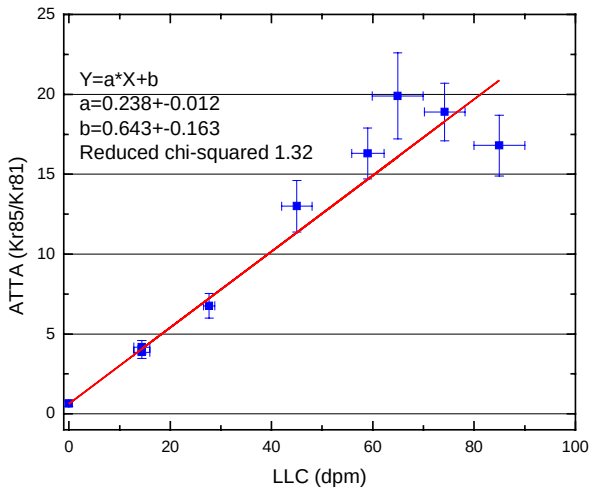

Figure 9.1 A comparison between ATTA and LLC. In ATTA, the ^{85}Kr/^{81}Kr ratios are measured. In LLC, the decay of ^{85}Kr are counted, and the unit is dpm/cc (decay per minute per cc STP of krypton).

There are a few things to be mentioned. First, Sample "O1" and "O3" are from the same krypton reservoir and the ratio measurements by ATTA are indeed consistent with each other. Therefore we can combine those two measurements to produce a more precise result 4.02 ± 0.29. Secondly, Sample "O2" is not a pure krypton gas, but a mixture of krypton gas and air due to a vacuum leak in the sample preparation system, which is both

measured by RGA in our vacuum system and confirmed by Bern group. Moreover, "O2" is not from the same krypton sample as the one measured by LLC, although the two krypton samples were collected by the Bern group on the same day. Therefore it is possible that the two samples had different ^{85}Kr abundances. We remove this point in the following data analysis. Thirdly, Sample "F2" is from a krypton reservoir that was collected by a German company between 1933 and 1940, therefore it is a pre-nuclear sample. The importance of this sample is that not only it serves as one data point in the test, but also it indicates the level of cross-contamination by measuring the ratio of ^{85}Kr/^{81}Kr since no ^{85}Kr is expected to be detectable in the pre-nuclear krypton gas. We did count ^{85}Kr atoms in this sample at the ^{85}Kr/^{81}Kr ratio level of 0.65 ± 0.17, or the level of 4% cross-contamination if we assume the contaminant is modern krypton. Our former cross-contamination measurement using RGA is approximately 2~3%. Therefore we assigned the cross-contamination level to be $4\% \pm 2\%$. The calibration of cross-contamination is expressed as follows (see also chapter 8),

$$r = r' + (r' - r^0)\varepsilon \qquad (9.2)$$

where r is actual ^{85}Kr/^{81}Kr ratio of the sample; r' is measured ^{85}Kr/^{81}Kr ratio of the sample; r^0 is the modern krypton ^{85}Kr/^{81}Kr ratio; ε is the cross-contamination level (here again we assume the contaminant is modern krypton).

After (1) combining "O1" and "O3"; (2) excluding "O2"; (3) correcting the systematical error due to the cross-contamination for each data point, the data points and the fitting curve are plotted out in Figure 9.2. Several conclusions can be drawn from the

figure. First, the linear correlation between $^{85}Kr/^{81}Kr$ ratios measured by ATTA and ^{85}Kr abundance measured by LLC demonstrated the validity of ATTA analysis. Secondly, the

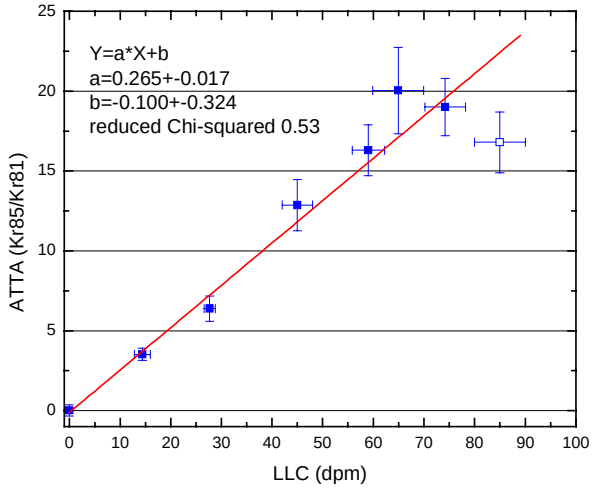

Figure 9.2 A comparison between ATTA and LLC after calibration of the cross-contamination effect (see the context).

^{81}Kr abundance can be derived from the slope of linear correlation if we assume that the system efficiencies for ^{85}Kr and ^{81}Kr are identical. The value is $(12.6 \pm 0.8) \times 10^{-13}$, which disagrees with the previous measurements (with LLC or AMS) by at least 5 standard deviations, as shown in Figure 9.3.

9.3 ^{81}Kr Abundance of Pre-Nuclear Krypton Sample

^{81}Kr abundances in the pre-nuclear krypton and post-nuclear krypton were expected to be identical, which were predicted by a detailed analysis of possible sources (see chapter 1) and confirmed by measurements with AMS. After we finished our double-blind test with LLC, we also did the measurement to compare the ^{81}Kr abundance of pre-nuclear

krypton gas and of post-nuclear krypton gas. A ~300 µl STP of pre-nuclear krypton sample was supplied by the Bern group. The sample was made from the same krypton reservoir as Sample "F2" and spiked with ^{85}Kr. Like the double blind test, the Bern group

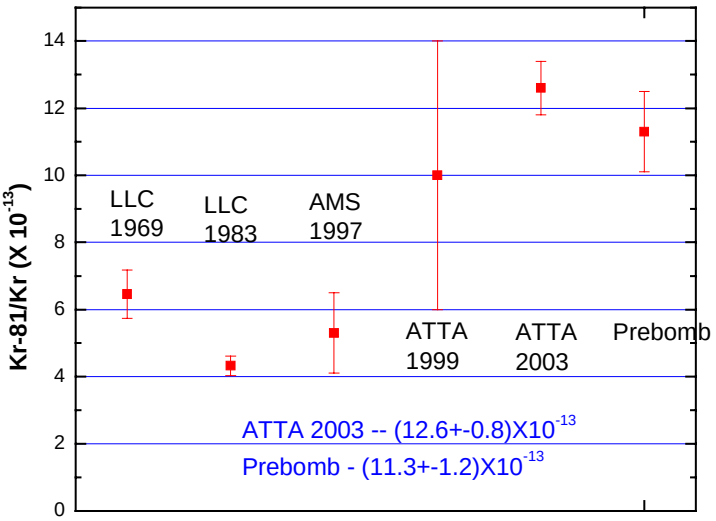

Figure 9.3 Comparison between ATTA result of ^{81}Kr/Kr and other measurements performed by LLC and AMS.

did LLC measurement of ^{85}Kr/Kr ratio and we did ATTA measurement of ^{85}Kr/^{81}Kr ratio (results are listed in Table 1). The LLC result is 81.2 ± 5 dpm/cc. ATTA result of ^{85}Kr/^{81}Kr ratio is 23.8 ± 2.0. The derived ^{81}Kr abundance is $(11.3 \pm 1.2) \times 10^{-13}$, which is consistent with ^{81}Kr abundance of modern krypton within one standard deviations (as shown in Figure 9.3).

10 ATTA ^{81}Kr-dating of the Ancient Groundwater of Nubian Aquifer in Western Egypt

With the success of double-blind test with LLC, we are in the position to apply our method on the real-world problems. The first application is to date the groundwater samples of Nubian Aquifer in Western Egypt. As we discussed in the previous chapters, ^{81}Kr-dating of these ancient groundwater samples will determine the residence time of the Nubian Aquifer, which could address a number of problems relating to the origin and history of the Nubian Aquifer. On the technical side, this work will further demonstrate the capability of our method in practical ^{81}Kr-dating and lead to other applications in environmental research.

10.1 Nubian Aquifer

Nubian Aquifer, one of the world's largest groundwater reservoirs, lies beneath the surface of the hyperarid Western Desert of Egypt, adjacent portions of eastern Libya, northeastern Chad and northwestern Sudan (shown in Figure 10.1). The area of the aquifer is approximately 2×10^6 km^2 and the volume of the aquifer is approximately 5×10^4 km^3, which is equivalent to 500 years of Nile River discharge.

The Nubian aquifer has two major basins: the Kufra Basin of Libya, northeastern Chad, and northwestern Sudan and the Dakhla Basin of Egypt. The aquifer reaches a depth of 3,000 m in the center of the Dakhla Basin. Groundwater of the Dakhla Basin area flows from southwest to northeast and discharge naturally at oases. The recharge of

the aquifer is minor compared with the discharge. Two models were proposed to explain the origin of the groundwaters: (1) large-scale flow from mountainous recharge areas in the southwest [60]; (2) recharge during previous more humid climatic conditions that prevailed throughout the present desert area [61].

On the basis of the existing ^{14}C data and ^{36}Cl data, it is believed that a significant fraction of the groundwater in the Nubian Aquifer may have a residence time longer than 400,000 years. The ^{36}Cl data cannot supply reliable age information mainly due to the uncertainties of $^{36}Cl/Cl$ data caused by the subsurface production of ^{36}Cl. The $^{81}Kr/Kr$ data, however, have the potential to resolve these fundamental issues and help understand the history of the aquifer.

10.2 Groundwater Sampling

The Nubian Aquifer groundwater sampling trip led by Neil Sturchio, a geologist at the University of Illinois at Chicago, was carried out in May, 2002.

Six groundwater samples for trace analysis of ^{81}Kr were collected at six wells in the Western Desert of Egypt, respectively (Figure 10.2). The sampling sites are: Kharga, Baris, El Zayat, Dakhla, Farafra and Bahariya (shown in Figure 10.1). Gases were extracted from 5 - 10 tons of water samples on site by spraying the water into the evacuated chamber and compressing the gas into gas cylinders (shown in Figure 10.3). The gas samples (each has a volume of approximately 300 liters STP) were shipped to the University of Bern for krypton separation and purification.

To complement the ^{81}Kr analyses and place them in a broader geochemical and isotopic context, a set of other chemical and isotopic analyses of the water samples has been and is being performed. Temperature and pH values of the water were recorded at each sampling site. The interpretation of all these data is out of the scope of this thesis and will be covered in a later publication.

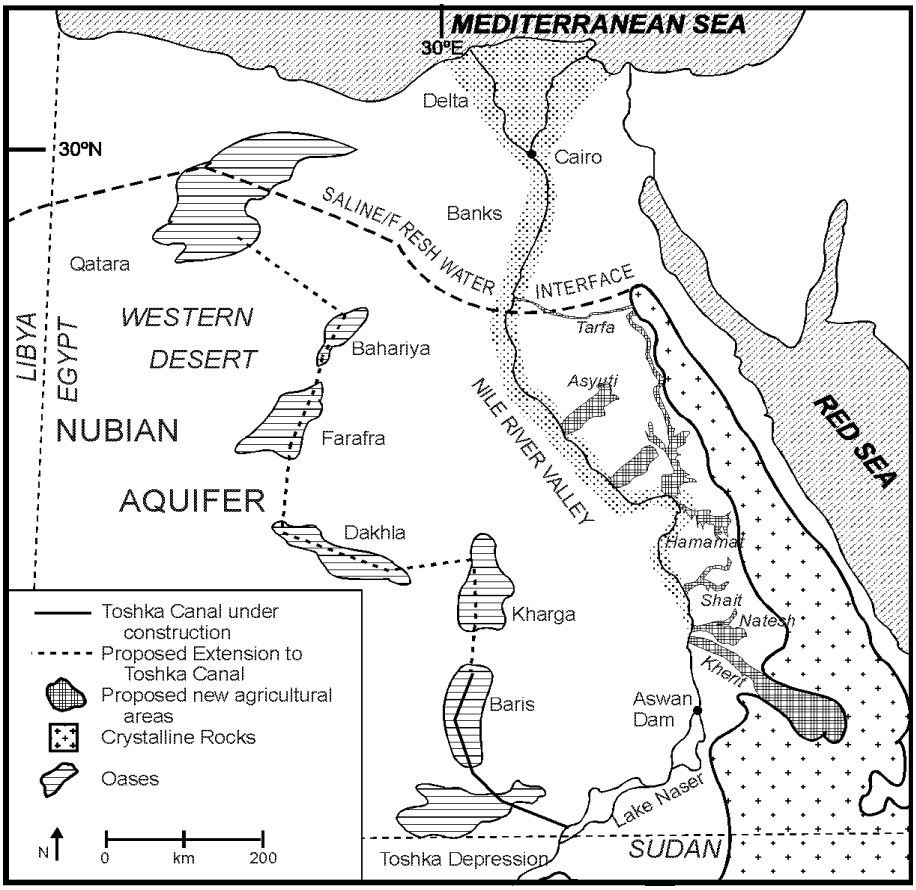

Figure 10.1 Location map showing the Nubian Aquifer. 5 oases are indicated in the map. The El Zayat oasis (not shown in the figure) locates between Dakhla and Kharga, near Dakhla.

10.3 Krypton Sample Preparation

At the University of Bern, a series of gas chromatographic and other separations were

Figure 10.2 Sampling site. The pipe connecting to the degassing machine was pushed deep into the well in order to avoid the contact of ancient groundwater with the atmosphere.

Figure 10.3 An automatic water degassing system developed at the University of Bern. At each sampling site, the typical water flow rate is 20 liters/minute and the degassing rate is approximately 20 cm^3 STP/liter of water.

performed to separate the krypton from the gas samples. Each krypton sample was

spiked with ^{85}Kr that serves as control isotope. For each sample, ^{85}Kr isotopic abundance was measured by LLC measurement. The spiked krypton samples (each has a volume of ~100 μl STP) were sealed in a steel container with a NuPro valve and sent to Argonne National Laboratory for ^{81}Kr analysis.

10.4 ^{81}Kr-dating: Procedures and Results

The procedures are the same as in the double-blind test (see Chapter 9).

So far, we have analyzed two of seven samples. The results are shown in Table 10.1.

Table 10.1 Experimental results of two water samples.

Sample	Volume (μl STP)	Used Volume (μl STP)	# of runs	# of ^{81}Kr	# of ^{85}Kr	Ratio of ^{85}Kr/^{81}Kr	LLC (dpm)
Farafra	82	40	15	5	181	109±49	80.5±8.1
Baris	500	120	34	29	773	80±15	80.5±8.1

We were informed by the group at University of Bern that the krypton sample were mixed with less than 10% of methane (CH_4). We did find that amount of methane, which had a negligible effect on the experiment. Meanwhile, we found a significant amount of helium in the sample (He/Kr ratio ~ 1:1). High helium pressure quenched the metastable krypton atoms and reduced the trap loading rate of krypton atoms. Now this problem has been solved by pumping the helium out of the sample container through the reservoir and

the vacuum system while keeping the krypton in the sample container with liquid nitrogen cooling. This can be realized because the boiling point of krypton (120 ^{0}K) is higher than nitrogen (77 ^{0}K) while helium (4.55 ^{0}K) is lower.

The Farafra sample size is 82 μl STP (including helium). We actually used approximately 40 μl STP of krypton. The sample was measured in 15 cycles. 5 counts of ^{81}Kr and 181 counts of ^{85}Kr were accumulated. Ratio of ^{85}Kr/^{81}Kr is 109±49.

For Baris sample, we used approximately 120 μl STP of krypton. In three experimental runs (34 cycles), 29 counts of ^{81}Kr and 773 counts of ^{85}Kr are accumulated. The ratio of ^{85}Kr/^{81}Kr is 80±15.

10.5 Data Aanlysis

Using Equation (8.4), we can derive the age information from the ratio of ^{81}Kr/^{85}Kr ratio (or ^{81}Kr isotopic abundance) in modern krypton to ^{81}Kr/^{85}Kr ratio (or ^{81}Kr isotopic abundance) in the water samples.

^{81}Kr isotopic abundance in modern krypton is $(12.6 \pm 0.8) \times 10^{-13}$ (see Chapter 9). ^{81}Kr isotopic abundance in water sample is derived from our measurement of ^{81}Kr/^{85}Kr ratio and LLC measurement of spiked ^{85}Kr isotopic abundance in the samples.

Cross-sample contamination level is 4% ± 2% (see Chapter 9).

The age information of the two samples is listed in Table 10.2.

Table 10.2 Two water sample age information.

Water Sample	^{81}Kr isotopic abundance (10^{-13})	Age (kyr)
Farafra	2.48±1.15	596±195
Baris	3.37±0.72	474±89

The results of the first two water samples setup a new milestone for ATTA - Radio-Krypton dating of ancient groundwater for the first time.

A comparison with ^{36}Cl data as well as sample measurements is necessary. It is beyond the scope of this thesis to give a hydrological interpretation of the results. However the preliminary ^{81}Kr result showed that the Baris sample is surprisingly old.

With the success of the first ^{81}Kr-dating of the ancient groundwater, we are very confident that more measurements of these two samples and other water samples will supply reliable age information on the groundwater in the Nubian Aquifer.

Reference

1. J. Arnold and W. Libby. Age determination by radiocarbon content: checks with samples of known age. Science **110**, 678 (1949).

2. W. Libby. Radiocarbon dating. Nobel Lecture, December 12, 1960.

3. W. Kutschera. Accelerator mass spectrometry: a versatile tool for research. Nucl. Instr. Meth. B **50**, 252 (1990).

4. P. Damon *et al.* Radiocarbon dating of the Shroud of Turin. Nature **337**, 611 (1989).

5. Isotopes of noble gases as tracers in environmental studies. (Vienna, Austria, 1989)

6. Edited by P. Cook and A. Herczeg. Environmental tracers in subsurface hydrology. (2000)

7. Edited by L. Currie. Nuclear and chemical dating techniques. (1982)

8. Edited by W. Alley. Regional ground-water quality. (1993)

9. J. Ahearne. Radioactive waste: the size of the problem. Physics Today Vol. **50**, No. 6, 24 (1997); K. Crowley. Nuclear waste disposal: the technical challenges. Physics Today Vol. **50**, No. 6, 32 (1997).

10. M. Apted *et al.* Yucca mountain: Should we delay?. Science **296**, 2333 (2002).

11. H. Oeschger. Accelerator mass spectrometry and ice core research. Nucl. Instr. Meth. B **29**, 196 (1987).

12. J. Petit *et al.* Climate and atmospheric history of the past 420,000 years from the Vostok ice core, Antarctica. Nature **399**, 429 (1999).

13. D. Schoen. Learning from polar ice core research. Environmental Science and Technology Vol. **33**, Issue 7, 160A (1999).

14. R. Alley and M. Bender. Greenland ice cores: frozen in time. Sci. Am. **266**, 80 (February, 1998).

15. A. Wilson and D. Donahue. AMS carbon-14 dating of ice: progress an future prospects. Nucl. Instr. Meth. B **52**, 473 (1990).

16. W. Broecher. Chaotic climate. Sci. Am. **263**, 62 (November, 1995).

17. W. Kutschera. Accelerator mass Spectrometry: analyzing our world atom by atom. AIP conference **495**, 407 (1999).

18. W. Kutschera *et al.* Long-lived noble gas radionuclides. Nucl. Instr. Meth. B **92**, 241 (1994).

19. F. Hippel, D. Albright and B. Levi. Stopping the production of fissile material for weapons. Sci. Am. **253**, 40 (1985).

20. H. Loosli. A dating method with ^{39}Ar. Earth Planet. Sci. Lett. **63**, 51 (1983).

21. W. Broecker and T. Peng. Comparison of ^{39}Ar and ^{14}C ages for waters in the deep ocean. Nucl. Instr. Meth. B 172, 473 (2000).

22. B. Lehmann. Counting radioactive noble gas atoms: lasers, accelerators or decay counters? Resonance Ionization Spectroscopy 2000, edited by J. Parks and J. Young (AIP, New York, 2001).

23. Edited by A. Jull *et al.* Methods of low-level counting and spectrometry. (IAEA, Vienna, 1981).

24. H. Loosli *et al.* Ten years low-level counting in the underground laboratory in Bern, Switzerland. Nucl. Instr. Meth. B **17**, 402 (1986).

25. H. Loosli and H. Oeschger. ^{37}Ar and ^{81}Kr in the atmosphere. Earth Planet. Sci. Lett. **7**, 67 (1969).

26. Proceedings of the 8th International Conference on Accelerator Mass Spectrometry. Nucl. Instr. Meth. B **172** (2001).

27. R. Muller. Radioisotope dating with a cyclotron. Science 196, 489 (1977).

28. D. Elmore and F. Phillips. Accelerator mass spectrometry for measurement of long-lived radioisotopes. Science 236, 543 (1987).

29. W. Kutschera. Accelerator mass spectrometry: a versatile tool for research. Nucl. Instr. Meth. B **50**, 252 (1990).

30. P. Collon *et al.* Measurement of ^{81}Kr in the atmosphere. Nucl. Instr. Meth. B **123**, 122 (1997).

31. P. Collon *et al.* ^{81}Kr in the Great Artsian Basin, Australia: a new method for dating very old groundwater. Earth Planet. Sci. Lett. **182**, 103 (2000).

32. P. Collon. A new method to detect cosmogenic ^{81}Kr. Ph.D. Thesis (University of Vienna, Austria 1999).

33. I. Ahmad *et al.* Ultra-high-sensitivity measurements and investigation of fundamental interactions. Physics Division Annual Report 2001, Argonne National Laboratory.

34. Private Communication with P. Collon.

35. G. Hurst *et al.* Method for counting noble gas atoms with isotopic selectivity. Rep. Prog. Phys. **48**, 1333 (1985).

36. B. Lehmann *et al.* An isotope separator for small noble gas samples. Nucl. Instr. Meth. B 28, 571 (1987).

37. N. Thonnard and R. Willis, M. Wright and W. Davis. Resonance Ionization Spectroscopy and the detection of ^{81}Kr. Nucl. Instr. Meth. B 29, 398 (1987).

38. B. Lehmann, H. Loosli, D. Rauber, N. Thonnard and R. Willis. ^{81}Kr and ^{85}Kr in groundwater, Milk River aquifer, Alberta, Canada. Appl. Geochem. **6**, 419 (1991).

39. W. Fairbank Jr. Photon burst mass spectrometry. Nucl. Instr. Meth. B **29**, 407 (1987).

40. W. Fairbank Jr. Photon burst mass spectrometry for the measurement of ^{85}Kr at ambient levels. SPIE **3270**, 174 (1998).

41. C.-Y. Chen, Y. Li, K. Bailey, T. O'Connor, L. Young and Z.-T. Zheng. Ultrasensitive isotope trace analysis with a magneto-optical trap. Science **286**, 1139 (1999).

42. Z.-T. Lu, K. Bailey, C.-Y. Chen, X. Du, Y. Li, T. O'Connor and L. Young. Atom trap trace analysis. Atomic Physics 17, edited by E. Arimondo, P. Denatale, and M. Inguscio (AIP 2001).

43. H. Metcalf and P. Straten. Laser cooling and trapping. (1999).

44. Edited by S. Chu and C. Wieman. Laser cooling and trapping of atoms. J. Opt. Soc. Am. B Vol. **6**, No. 11 (1989).

45. W. Phillips. Laser cooling and trapping of neutral atoms. In Laser Manipulation of Atoms and Ions, edited by E. Arimondo, W. Philipps, and F. Strumia, Proceedings of the International School of Physics "Enrico Fermi".

46. W. Phillips, J. Prodan and H. Metcalf. Laser cooling and electromagnetic trapping of neutral atoms. J. Opt. Soc. Am. B Vol. **2**, 1751 (1985).

47. W. Ertmer, R. Blatt, J. Hall and M. Zhu. Laser manipulation of atomic beam velocities: demonstration of stopped atoms and velocity reversal. Phys. Rev. Lett. **54**, 996 (1985).

48. W. Phillips and H. Metcalf. Laser deceleration of an atomic beam. Phys. Rev. Lett. **48**, 596 (1982)

49. E. Raab, M. Prentiss, A. Cable, S. Chu and D. Pritchard. Trapping of neutral sodium atoms with radiation pressure. Phys. Rev. Lett. **59**, 2631 (1987).

50. A. I. Ludin and B. E. Lehmann. High-resolution diode-laser spectroscopy on a fast beam of metastable atoms for detecting very rare krypton isotopes. Appl. Phys. B **61**, 461 (1995).

51. B. D. Cannon. Hyperfine spectra of the radioactive isotopes ^{81}Kr and ^{85}Kr. Phys. Rev. A **47**, 1148 (1993)

52. A. S. Arnold, J. S. Wilson and M. G. Boshier. A simple extended-cavity diode laser. Rev. Sci. Instr. **69**, 1236 (1998).

53. C. E. Wieman and L. Hollberg. Using diode lasers for atomic physics. Rev. Sci. Instr. **62**, 1 (1991)

54. H. R. Telle. Injection locking of a 1.3 μm laser diode to an $LiNdP_4O_{12}$ laser yields narrow linewidth emission. Electron. Lett. **22**, 150 (1986)

55. A. Corney. Atomic and Laser Spectroscopy (1977)

56. J. F. Kelly and A. Gallagher. Efficient electro-optic modulator for optical pumping of Na beams. Rev. Sci. Instr. **58**, 563 (1987)

57. C.-Y. Chen *et al.* Beam of metastable krypton atoms extracted from a rf-driven discharge. Rev. Sci. Instr. **72**, 271 (2001)

58. W. Rooijakkers, W. Hogervorst and W. Vassen. An intense collimated beam of metastable helium atoms by two-dimensional laser cooling. Opt. Commun. **123**, 321 (1996)

59. V. V. Kuzminov and A. A. Pomanski. Radiocarbon **22**, 311 (1980)

60. J. Ball. Geographical Journal **70,** 21 (1927)

61. U. Thorweihe. Hydrogeologie des Dakhla Berkens (Agypten). Berliner Geowiss. Abh. A**38**, 1 (1982)